Review Article

ADVANCED PHOTONICS

Power consumption of light engines for emerging augmented reality glasses: perspectives and challenges

Yizhou Qian, Zhiyong Yang, Sung-Chun Chen, Yongziyan Ma, Yi-Chien Chen, Hsueh-Shih Chen, Chih-Lung Lin, and Shin-Tson Wu*
University of Central Florida, College of Optics and Photonics, Orlando, Florida, United States

Abstract. Lightweight augmented reality (AR) eyeglasses have been increasingly integrated into human daily life for navigation, education, training, healthcare, digital twins, maintenance, and entertainment, just to name a few. To facilitate an all-day comfortable wearing, AR glasses must have a small form factor and be lightweight while keeping a sufficiently high ambient contrast ratio, especially under outdoor diffusive sunlight conditions and low power consumption to sustain a long battery operation life. These demanding requirements pose significant challenges for present AR light engines due to the relatively low efficiency of the optical combiners. We focus on analyzing the power consumption of five commonly employed microdisplay light engines for AR glasses, including micro-LEDs, OLEDs, liquid-crystal-on-silicon, laser beam scanning, and digital light processing. Their perspectives and challenges are also discussed. Finally, adding a segmented smart dimmer in front of the AR glasses helps improve the ambient contrast ratio and reduce the power consumption significantly.

Keywords: augmented reality; microdisplays; power consumption.

Received Oct. 28, 2024; revised manuscript received Jan. 23, 2025; accepted for publication Feb. 28, 2025; published online Mar. 28, 2025.

[DOI: 10.1117/1.AP.7.3.034001]

1 Introduction

Lightweight augmented reality (AR) smart glasses are emerging and have been gradually integrated into human life for navigation, education, training, healthcare, maintenance, and entertainment, just to name a few. As AR devices strive to become more compact for all-day comfortable wearing, minimizing power consumption is essential to extend the battery life and reduce thermal effect while maintaining high image quality. Light engines, responsible for generating and projecting images onto the AR display, often account for a substantial portion of the total power usage.[1] Figure 1(a) depicts a waveguide-based AR device structure. The light from the microdisplay is collected by a projection lens, coupled into the waveguide through an in-coupler, propagating in the waveguide by total internal reflection (TIR), and then coupled out to human eyes.[3,4] Nevertheless, a significant loss happens during this process resulting from the light leakage and angular-dependent diffraction efficiency of the in-coupler and out-coupler, absorption and scattering losses during TIR, and duplication from exit pupil expansion (EPE).[5] Presently, to achieve a 30-deg field-of-view (FoV), the diffractive waveguide efficiency is limited to ~3%, or 1300 nits/lm. However, under daylight conditions, the outdoor illuminance can achieve $>$ 14,000 lux. As a result, a ~4000-nit luminance to the eye is required to distinguish the projected image from the ambient light,[6] which implies the light engine must deliver 3-lm luminous power to the in-coupler.

In addition to battery life, the thermal effect of the AR glasses is another concern. Figure 1(b) shows the temperature rise near the ear when the power consumption increases from 1, 5, to 10 W.[2] Given the additional power demands from components such as the CPU, GPU, and Wi-Fi module,[7] the power consumption of each microdisplay panel should be capped at 1 W.

The objective of this review paper is to provide a comprehensive analysis of the efficiency and power consumption of five commonly used light engines in current AR devices. We

---

*Address all correspondence to Shin-Tson Wu, swu@creol.ucf.edu

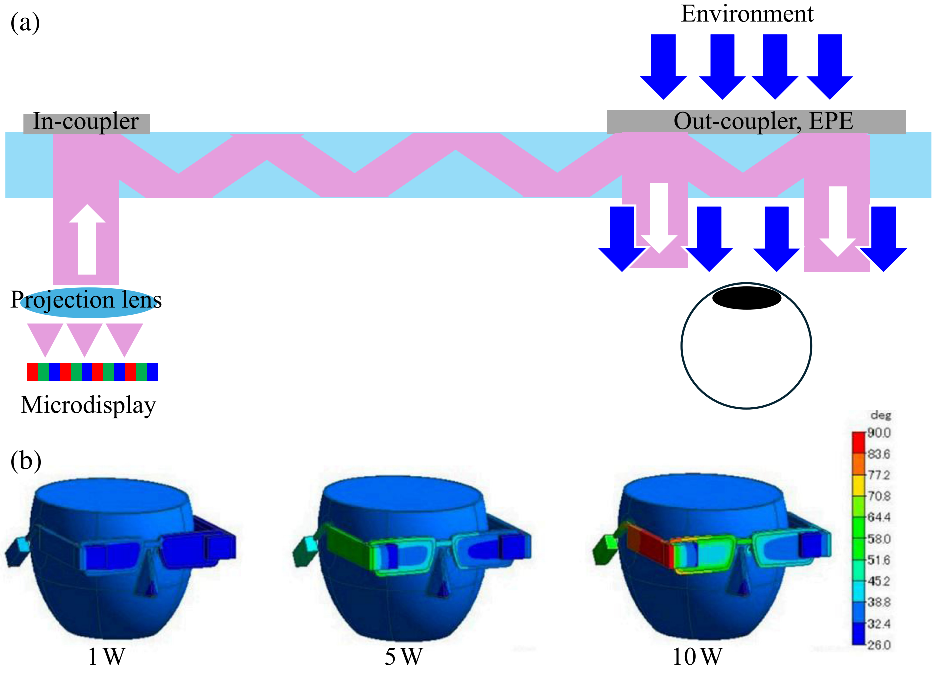

Fig. 1 (a) Working principle of diffractive waveguide-based AR device. (b) Temperature distribution at different power consumption. Reprinted from Ref. 2 under a Creative Commons license.

begin with two emissive displays: micro-LED (μLED) and micro-OLED (μOLED), focusing on their distinct approaches to achieving high-resolution full-color displays. Next, we will highlight the working principles and power efficiency improvements of two reflective light modulation microdisplays: liquid-crystal-on-silicon (LCoS) and digital light processing (DLP). Afterward, we will discuss the high-efficiency laser beam scanning (LBS) technology and then compare the power consumption of these waveguide-based AR light engines using a 3-lm light source whose radiation pattern is confined within ± 15 deg when displaying different image contents. Finally, adding a segmented smart dimmer helps improve the ambient contrast ratio and reduce power consumption significantly.

2 μLED

2.1 Working Principle

Light-emitting diode (LED) is an inorganic semiconductor device that emits light when an electric current passes through its p-n junction. This junction consists of an n-type region, doped with extra electrons, and a p-type region, doped with extra holes. When a positive voltage is applied to the LED, electrons in the conduction band (E_c) of the n-type semiconductor and holes in the valence band (E_v) of the p-type semiconductor move towards the active region, where they recombine to form excitons [Fig. 2(a)]. This recombination can proceed via two processes: non-radiative and radiative. The non-radiative recombination channels include Shockley-Read-Hall (SRH) recombination, which results from carrier trapping at crystal defects, and Auger recombination, where the recombination energy is transferred to a third carrier, leading to heat dissipation.[9] The radiative recombination leads to photon emission, generating light at a frequency $\nu = E_g/h$, where E_g is the energy band gap and h is Planck's constant.

μLEDs are LEDs with a chip size smaller than 50 μm and have found wide range applications, including modular large-screen televisions (panel size $> 75''$), transparent displays, and microdisplays.[10] For ultra-high resolution density AR applications, the μLED pixel size is usually smaller than 4 μm, and the complementary metal-oxide-semiconductor (CMOS) backplane technology is required for the driving circuits in an active-matrix (AM) μLED display.[11]

To activate an AM μLED panel, two driving methods are commonly used: pulse amplitude modulation (PAM) and pulse width modulation (PWM). For PAM, the driving circuits can be quite compact, consisting of two transistors and one capacitor (2T1C).[12,13] However, μLED's emission wavelength and external quantum efficiency (EQE) vary under different driving current densities, leading to wavelength shift and increased power consumption at low gray levels when adopting the PAM driving method. By contrast, the PWM driving method keeps the driving current fixed and modulates the gray level by adjusting the emission time. PWM can be categorized into analog and digital types, depending on different data input methods and pixel circuits. Typically, analog PWM requires a sawtooth-like sweep signal generated from the external driver integrated circuit (IC) or internal circuit.[14,15] The driving transistor operates in the saturation region as a current source, determining the μLED's driving current. The drain-to-source voltage (V_{DS}) is relatively high (~5 V), which increases the voltage across V_{DD} to V_{SS} (~8.5 V) and leads to a higher power consumption.[14,16] Figure 2(b) describes a basic 3T1C subpixel circuit for PWM.[8] For digital PWM, the driving transistor M_2 operates in the linear region, functioning as an on/off switch, depending on the input data level. Therefore, the power consumption of driving transistors in digital PWM is much less than that in analog PWM. The data input time for each pixel is dependent on the display's bit depth, as described in Fig. 2(c), and higher bit depths require increased data driver IC frequencies, leading to higher power consumption.[17]

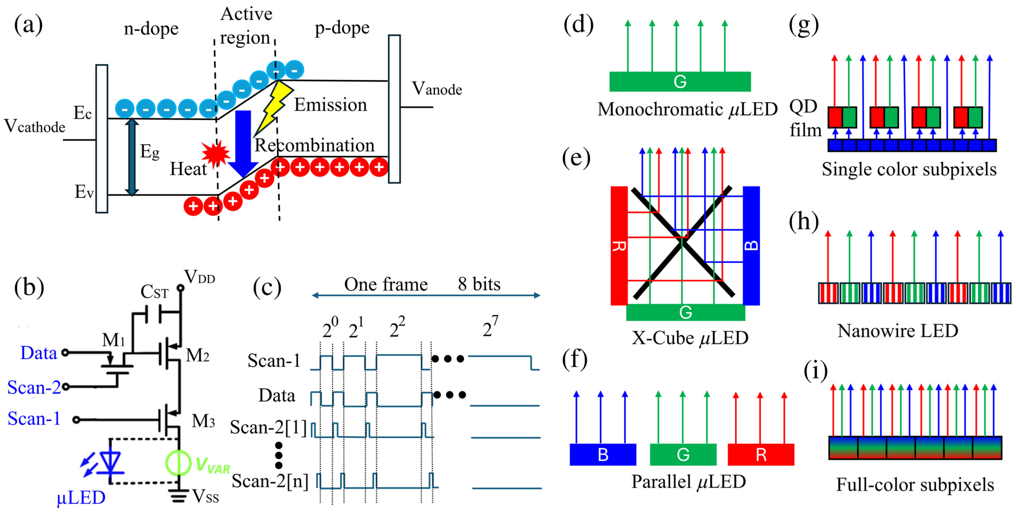

Fig. 2 (a) Working principle of LED. (b) 3T1C circuit for PWM driving. Adapted with permission from Ref. 8, © Optica 2021. (c) Digital PWM input data. (d)–(i) Schematic of (d) monochromatic, (e) X-cube, (f) parallel, (g) QDCC, (h) nanowire, and (i) full-color-subpixel μLED.

The total power consumption of a μLED panel with digital PWM driving consists of four parts:

$$P = (P_{\mathrm{LED}} + P_{\mathrm{MOS}}) \times \mathrm{Resolution} \times \eta_{\mathrm{Duty}} + P_{\mathrm{data}} + P_{\mathrm{scan}} + P_{\mathrm{IC}}, \tag{1}$$

$$P_{\mathrm{scan}} = \mathrm{Row} \times C_{\mathrm{row}} \times V_{\mathrm{scan}}^2 \times \mathrm{bits} \times f, \tag{2}$$

$$P_{\mathrm{data}} = \mathrm{Col} \times (C_{\mathrm{col}} + C_{\mathrm{ST}}) \times V_{\mathrm{data}}^2 \times (f \times \mathrm{Row} \times \mathrm{bits}), \tag{3}$$

where P_{LED}, P_{MOS}, P_{scan}, P_{data}, and P_{IC} represent the power consumption of the individual μLED chip, transistors (M_2, M_3), scan line, data line, and peripheral integrated circuit (IC), respectively. During simulation, we assume that the scan voltage (V_{scan}) and the data voltage (V_{data}) are 5V and 4V, respectively, in reference to V_{SS}. In Eq. (1), η_{Duty} refers to the duty ratio, which is defined as the pixel-on time in each frame, and its value is dependent on the required luminous power. The typical P_{IC} under resolution of 640×480 is about 40 to 60 mW when all pixels are off.[18] In Eqs. (2) and (3), f and bits denote the frame rate and the bit depth of the display, and C_{row}, C_{col}, and C_{ST} correspond to the capacitances of row wire, column wire, and storage capacitor, respectively. In our simulations, we assume $C_{\mathrm{row}} = 300$ fF, $C_{\mathrm{col}} = 300$ fF, and $C_{\mathrm{ST}} = 30$ fF.[14,19]

The total optical power emitted from a μLED chip is related to its wall-plug efficiency (WPE) and EQE as[10]

$$P_{\mathrm{Optical}} = \mathrm{WPE} \times P_{\mathrm{LED}} = \mathrm{EQE} \times \frac{hc}{e\lambda V_{\mathrm{LED}}} \times V_{\mathrm{LED}} I_{\mathrm{LED}} = \mathrm{EQE}\frac{hcI_{\mathrm{LED}}}{e\lambda}, \tag{4}$$

where h, c, e, and λ represent the Planck's constant, speed of light in vacuum, electron charge, and emission wavelength, respectively.

In an AR glass, the acceptance angle of the projection lens is typically within ±15 deg, whereas the light emission from the µLED is Lambertian. To increase the coupling efficiency of μLED into the imaging system, a microlens array is often laminated on top of the μLED array for a better collimation.[20] The η_{Duty} dependence on the luminous power ϕ (unit: lumen) provided by a μLED chip can be calculated as

$$\eta_{\mathrm{Duty}} = \frac{\phi}{P_{\mathrm{Optical}} \times \eta_{AP} \times \eta_{15} \times N}, \tag{5}$$

$$\eta_{15} = \frac{\int_0^{15} I_{\mathrm{Optical}}(\theta)\mathrm{d}\theta}{\int_0^{90} I_{\mathrm{Optical}}(\theta)\mathrm{d}\theta}, \tag{6}$$

$$N = \int_{400\mathrm{nm}}^{700\mathrm{nm}} S(\lambda)K(\lambda)\mathrm{d}\lambda, \tag{7}$$

where η_{AP} ($\approx 70\%$) is the aperture ratio of the microlens array,[21] η_{15} ($\approx 62\%$) is the luminous intensity ratio confined within ± 15 deg,[20] $I_{\mathrm{optical}}(\theta)$ is the luminous intensity dependence on the polar angle, S represents the μLED spectrum distribution, and K is the spectral human eye sensitivity function.

In the following sections, we will introduce and analyze various commercial μLED technologies, including monochromatic μLED [Fig. 2(d)], X-cube μLED [Fig. 2(e)], parallel RGB μLEDs [Fig. 2(f)], and quantum dot color conversion (QDCC) μLED [Fig. 2(g)]. In addition, we will explore the potential of several emerging high-resolution μLED technologies, such as nanowire LED [Fig. 2(h)] and full-color subpixel μLED [Fig. 2(i)].

2.2 Monochromatic μLED

The fabrication of monochromatic μLED involves monolithic integration technology such as wafer bonding and flip-chip bonding without mass transfer as shown in Figs. 3(a) and 3(b), respectively.[22] For wafer bonding, μLED epi wafer and CMOS wafer are first bonded through metal layers, then the pixels are formed by inductively coupled plasma reactive ion etching (ICP-RIE) and surface passivation. Nevertheless, the light extraction efficiency (LEE) is typically lower for the inverted trapezoidal structure due to the unavoidable shadow effect during the etching process.[1] By contrast, with flip-chip bonding, the pixels are formed prior to bonding. However, this method

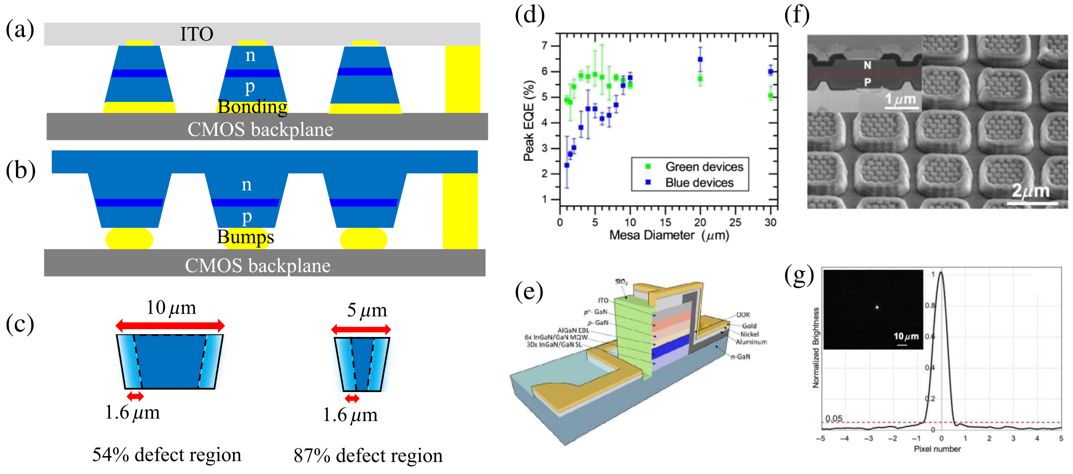

Fig. 3 (a) Wafer bonding. (b) Flip-chip bonding. (c) Percentage of defect regions in μLED. (d) Measured size-dependent peak EQE of μLEDs on wafer. Adapted with permission from Ref. 24, © AIP Publishing 2020. (e) ALD surface passivation. Reprinted with permission from Ref. 27, © Optica 2018. Continuous MQW μLED: (f) structure and (g) optical crosstalk. Reprinted with permission from Ref. 33, © John Wiley and Sons 2024.

requires precise alignment, which limits its applicability to high-resolution density AR displays.

For both wafer bonding and flip-chip bonding, ICP-RIE dry etching has been widely applied to precisely control the μLED mesa size. However, the high-energy ions in the plasma cause material damage, especially at the sidewalls, resulting in an increased non-radiative recombination rate and leakage current.[23] As the μLED size continues to shrink, the increased surface-to-volume ratio leads to a higher percentage of the defect region, as Fig. 3(c) illustrates. Therefore as Fig. 3(d) depicts, the EQE of μLED is highly dependent on the chip size due to sidewall defects.[24] Various methods have been proposed to mitigate these material defects. In 2009, Yang et al. proposed a potassium hydroxide (KOH) wet etching method after dry etching to remove the defect area in GaN-based LEDs.[25] In addition, surface passivation by dielectric atomic layer deposition (ALD) has been investigated to reduce the dangling bonds of gallium and nitrogen atoms.[26] In 2018, Wong et al. improved the surface passivation by replacing conventional PECVD with ALD of the SiO_2 passivation layer in Fig. 3(e), increasing the EQE of a 20 μm × 20 μm μLED from 24% to 33%.[27] Later, in 2019, the same group reported a size-independent EQE of 23% for blue μLEDs down to 10 μm × 10 μm by combining KOH chemical treatment with ALD surface passivation.[28] Furthermore, a proper electrode design can also avoid the defect regions.[29] For example, Hsu et al. improved the current confinement effect on a blue 10 μm × 10 μm μLED array and achieved an optimized EQE of 9.95% by modifying the electrode contact size to 5 μm × 5 μm.[30] Several novel designs can avoid defects induced by ICP etching. For instance, bottom-up fabrication processes through selective epitaxy growth can avoid sidewall damage.[31,32] Another example is that, in 2024 SID Display Week, Jade Bird Display reported a novel continuous MQW AlGaInP red μLED design [Fig. 3(f)] to achieve a 4× higher power efficiency than conventional one.[33] However, optical crosstalk [Fig. 3(g)] degrades image quality and causes blurring.

A μLED's EQE may diminish after bonding to the panel due to misalignment and increased black matrix aspect ratio, which becomes more pronounced as resolution density rises. The wavelength and size-dependent EQEs are plotted in Fig. 4(a). In 2022, Wu et al. developed a 1920 × 1080 resolution blue μLED panel with a mesa diameter of 5 μm, achieving EQE of 6.5% at a current density of 10.2 A/cm^2 and a peak wavelength of ∼440 nm.[34] Typically, green μLEDs would exhibit a lower EQE than the blue ones because they require a higher indium concentration to reduce the bandgap. However, the increased indium content leads to a greater lattice mismatch between InN and GaN, reducing crystal quality. Despite this, green μLEDs with ultra-small mesa sizes can outperform blue μLEDs in efficiency, as the size-dependent non-radiative surface recombination rate for indium is less significant than for gallium.[24] In 2024, Wu et al. fabricated a 0.39-in. green μLED panel and achieved 7.17% peak EQE for green μLEDs with a mesa size of 5 μm.[35] For InGaN red μLEDs, the even richer indium concentration further reduces the EQE. As Feng et al. reported in 2022, the peak EQE of 2-μm InGaN red LEDs fabricated by selective epitaxy growth is only 1.75% on a wafer at ∼100 A/cm^2.[39] In addition, the broadened FWHM (full width at half maximum) due to inhomogeneous indium distribution and carrier localization reduces the color purity.[40] Alternatively, AlInGaP red LED can achieve a wider color gamut and higher EQE for large LEDs (e.g., >100 μm), but the efficiency drops significantly as the size decreases.[41] In 2022, Wu et al. fabricated a red AlGaInP μLED panel with a 10-μm mesa size, achieving an EQE of 5.3% at a current density of 500 A/cm^2.[42]

Due to its high sensitivity to human vision and superior efficiency at ultra-small pixel sizes, green InGaN/GaN LED is the favored choice for lightweight monochromatic AR glasses, such as the Even Realities G1, which weighs only 40 g. The power consumption of the green μLED with 4 μm pixel pitch at three-lumen brightness is depicted as the green line in Fig. 4(b), which increases with the average pixel lit (APL) linearly. The power consumption at APL = 0% is about 50 mW, which is attributed to the high power consumption of the driving IC.[43] This method helps simplify the circuit design; however, the tradeoffs are reduced image quality and increased power consumption in the low APL region.

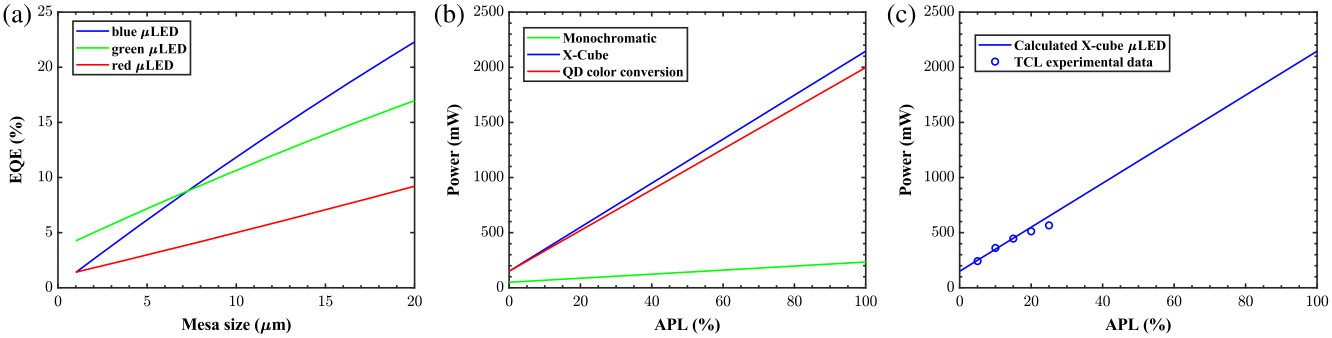

Fig. 4 (a) Size-dependent μLED EQE on panel.[24,33–38] (b) Calculated power consumption of 640 × 480 μLED panels with a subpixel size of 4 μm to provide 3-lm luminous power to the in-coupler. (c) Power consumption comparison between the calculated X-cube 3-panel μLEDs and measured TCL RayNeo X2 when producing 2-lm luminous power.

2.3 3-panel RGB μLEDs

At the present stage, integrating full-color μLEDs with CMOS onto a single display panel without mass transfer remains a challenge.[44] Although monolithic integration of full-color μLED can be achieved by multiple bonding processes,[45] its circuit design, pixel alignment, and angular color shift are the main problems. Thus far, the most mature commercial technology is to implement three monolithic RGB μLED panels as Figs. 2(e) and 2(f) show.

At the 2023 Display Week, JBD introduced an X-cube-based μLED "Hummingbird" projector, which integrates three RGB monochromatic panels using spatial integration through dichroic mirrors.[46] This compact design, with a volume of merely 0.4 cc for a 640 × 480 display panel, achieves a full-color pixel pitch of 4 μm and weighs only 1 g, making it a successful commercial product currently available. For instance, TCL RayNeo X2 AR glasses utilize the X-cube μLED projector and a diffractive waveguide to achieve 1500-nit brightness and 25 deg FoV. The next generation RayNeo X3 uses a similar design, and the weight is reduced from 120 to 70 g. However, the RGB pixel alignment is challenging for these high-resolution display panels. In 2024, Meta Orion AR glasses integrate three parallel μLED panels with a SiC waveguide ($n \approx 2.66$ at $\lambda = 550$ nm), and the device only weighs 98 g. Such a design alleviates the misalignment issue and further reduces the volume, although it increases the complexity and cost of the waveguide design.

To fairly compare the power consumption of full-color microdisplay light engines, we consider a 3-lm white light source consisting of RGB colors at 4:10:1 mixing ratios.[47] The optical power of the RGB μLEDs and the luminous power of the white light (ϕ_W) can be expressed as

$$P_{\mathrm{Optical},(R,G,B)} = \mathrm{EQE}_{(R,G,B)} \frac{hcI_{\mathrm{LED},(R,G,B)}}{e\lambda_{(R,G,B)}}, \tag{8}$$

$$\phi_W = \phi_R + \phi_G + \phi_B = 3\ \mathrm{lm};\ \phi_R : \phi_G : \phi_B = 4:10:1. \tag{9}$$

The calculated APL-dependent power consumption is plotted in Fig. 4(b), and it is significantly higher than that of green μLED displays due to the lower EQE of red μLEDs. The duty ratio for the RGB μLEDs is 25%, 7%, and 15%, respectively. To validate our calculation, we compare the calculated power consumption of a 2-lm X-cube μLED (blue line) to the experimental data from the TCL RayNeo X2 light engine (blue dots) in Fig. 4(c). The agreement is reasonably good (within 20%), considering such a sophisticated system, including RGB μLED materials, chip size effects, driving currents, and optics. Moreover, the power consumption data of μLED are rarely reported in the literature, especially at a specific APL.

2.4 Quantum Dot Color Conversion (QDCC) μLED

Quantum dot color conversion (QDCC) technology holds significant promise in modern display applications, especially when paired with μLED technology. The core mechanism involves using blue μLEDs to excite QDs, which convert a portion of the blue light into red and green. This method not only enhances the color purity for a wide color gamut but also eases the mass transfer of μLEDs, leading to reduced manufacturing cost and improved display resolution.[48] At 2024 Display Week, PlayNitride demonstrated a 0.49-in. μLED display with 4536 pixels-per-inch (PPI), over 100,000-nit luminance, and 106% NTSC color space with color filters.[49]

However, despite these attractive features, QDCC technology faces several technical barriers, particularly in addressing degradation caused by blue light excitation. First, prolonged exposure to blue light can degrade the optical properties of QDs, lowering the conversion efficiency and shortening the device's lifespan. This degradation is primarily due to the formation of photo-generated electrons and holes, which in turn accelerates the photo-oxidation and deterioration of the QD emissive layer. Several strategies have been developed to enhance QD stability, including surface ligand passivation,[50] core-shell engineering,[51] surface encapsulation,[52] and material development of heavy metal-free QDs. Second, there is a tradeoff between color purity and energy efficiency. Although QDs offer excellent color purity, maintaining a proper balance between energy conversion efficiency and display color purity during the light conversion process can be challenging. Third, the optical properties of QDs are highly sensitive to their size and size distribution, which must be precisely controlled to maintain a consistent performance. Large-scale manufacturing of high-resolution QDCCs requires precision in the coating or photo-lithography process to ensure even distribution of the QDs. To minimize the QDCC film thickness, additional optical coatings, such as scattering particles or distributed Bragg reflectors (DBRs), are required.[53]

Considering a QDCC display excited by blue μLEDs, the optical power consumption for green and red pixels can be calculated as

$$P_{\text{Optical},(R,G)} = \text{EQE}_B \frac{hcI_{\text{LED},B}}{e\lambda_B} \times \eta_{\text{PCE},(R,G)}. \tag{10}$$

As reported by Nanosys, the power conversion efficiency η_{PCE} can achieve 38% for both red and green heavy-metal-free QDs.[54] The power consumption for a 3-lm output is plotted as the red line in Fig. 4(b). Here, the duty ratio of the RGB QDCC μLEDs is 33%, 17%, and 15%, respectively. The power consumption of QDCC μLED is slightly lower than that of X-cube–based μLED because of the higher efficiency of red subpixels. However, the short lifetime of green-emitting QDs and reduced quality of QD film for microdisplays are major concerns.[55]

2.5 Emerging μLED Technology

The III-nitride bottom-up nanowire LED is epitaxially grown layer-by-layer on a substrate using atomic self-assembly methods.[56,57] The selective area growth utilizes an etched template, and the nanowires are grown on a constrained area by metal-organic vapor-phase epitaxy (MOVPE), which can achieve precise control of nanowires.[58,59] The dopant incorporation is accomplished during the growing process without the etching process (which causes extra damage) to improve internal quantum efficiency.[60] Furthermore, the vertical structure behaves as a waveguide, which helps to boost the LEE and then EQE of nanowire µLEDs.[61] For example, Aledia announced a blue core-shell nanowire µLED with 32% EQE grown by bottom-up method.[62] To date, red and green nanowire µLEDs can achieve an EQE of 8.3%[32] and 25.2%,[63] respectively. However, the demanding fabrication procedure, challenging integration to CMOS backplane, and broad emission spectrum from red InGaN nanowire LEDs remain major barriers.

Integrating RGB colors into one subpixel can potentially triple the resolution density. The first approach is color tunable μLED,[64] and its emission wavelength from InGaN MQW is controlled by varying the indium concentration in different regions. In 2022, Protech introduced a dynamic pixel tuning technology that enables each pixel to emit different colors by adjusting the current density directly. A similar concept is applied in the V-groove color-tunable μLED, where the subpixels emit different colors by increasing the current density, ranging from 1 A/cm^2 to 80 A/cm^2,[64,65] respectively. However, the WPE of red, green, and blue is limited to 0.6%, 3%, and 1%, respectively. Ideally, a specific color corresponds to a specific current density. However, any variation in current would lead to luminance fluctuation, which requires color detection and demanding pulse width control. Furthermore, designing the active-matrix electrical backplane is highly complex due to the production yield challenges of each LED. A simpler approach is to employ time-sequential RGB colors, whereas low brightness for red, color breakup, and reduced color gamut remains to be overcome.

Alternatively, three independent RGB p-n junctions can be vertically stacked and driven independently to triple the pixel density.[66,67] In 2023, Shin et al. demonstrated a full-color vertical stacked μLED panel with a 9-μm pixel pitch.[68] To avoid unwanted photoluminescence, wavelength-selective polyimide (PI) absorbers are laminated between each layer as color filters and adhesive interlayers, but the LEE is compromised. Jin et al. proposed to use DBR as a bonding layer to recycle the downward light, as a result, the luminous efficiency of the white color is enhanced by 1.6% to 7.4%,[69] but the light leakage at large angle incidence and photoluminescence is unavoidable. In addition, the degraded color performance, demanding alignment accuracy, and complex active-matrix circuit design are existing challenges.

3 µOLED

3.1 Tandem Structures

Tandem μOLED on a silicon CMOS backplane is emerging as a promising self-emissive light engine for AR devices due to its high-resolution density and mature fabrication process. In conventional μOLED structures [Fig. 5(a)], electrons and holes are injected from the electron transport layer (ETL) and hole transport layer (HTL), respectively, leading to electron-hole pair recombination within the emissive layer (EML) and subsequent light emission. By contrast, tandem μOLED introduces an additional charge generation layer (CGL) between two or more EMLs.[72,73] The n-type CGL generates and transfers electrons to the lowest unoccupied molecular orbital (LUMO) of EML-1, whereas the p-type CGL generates and transfers holes to the highest occupied molecular orbital (HOMO) of EML-2. This CGL effectively acts as an internal electrode, enabling electron-hole recombination in both EMLs of the tandem μOLED, thereby enhancing light emission, as depicted in Fig. 5(b).

High-resolution tandem white μOLED displays can achieve a pixel density exceeding 3000 PPI, as the pixel structure is formed using color filters, as shown in Fig. 5(c). Such a high-resolution density is made through photolithography, whereas the use of color filters reduces the optical efficiency by more than 70%.[74] In 2018, Sony developed a 0.5″ white μOLED display with a 6.3 μm pixel pitch. They addressed the angular color shift by integrating an on-chip color filter and reduced driving voltage using a 4T2C circuit design.[75] However, the peak luminance of this display was limited to 2000 nits, making it unsuitable for AR eyewear. In 2024, LG Display introduced a 1.3″ full-color 3-stacked white μOLED panel with a 4175-PPI resolution density and a luminance efficiency of 38 cd/A.[70] Despite the high pixel density, the display operates at 11 V, and its peak brightness is constrained to 10,000 nits at a current density of 50 mA/cm^2. The device is intended for mixed reality applications, but the 10,000 nits brightness is still inadequate for AR glasses in bright ambient.

As illustrated in Fig. 5(d), RGB μOLED can obtain a higher light efficiency if the color filters can be eliminated. The ETL, HTL, and CGL can be uniformly applied across the RGB subpixels, simplifying the fabrication processes,[71] though additional color filters are still required on top of the structure to reduce optical crosstalk. Alternatively, the ETL, HTL, and CGL can be designed individually for each subpixel, with a black matrix inserted between subpixels to minimize crosstalk.[76] The primary challenge with RGB μOLED technology is to achieve high resolution. To pattern and define high-density subpixels, fine metal masks (FMMs) are necessary. However, FMMs must maintain strong mechanical stability to avoid sagging and pixel edge blurring. A thicker FMM, although more stable, introduces a shadow effect during fabrication, degrading pixel quality. To overcome this, APS Corp. has demonstrated a laser-patterned, thin-film FMM that achieves resolutions greater than 3000

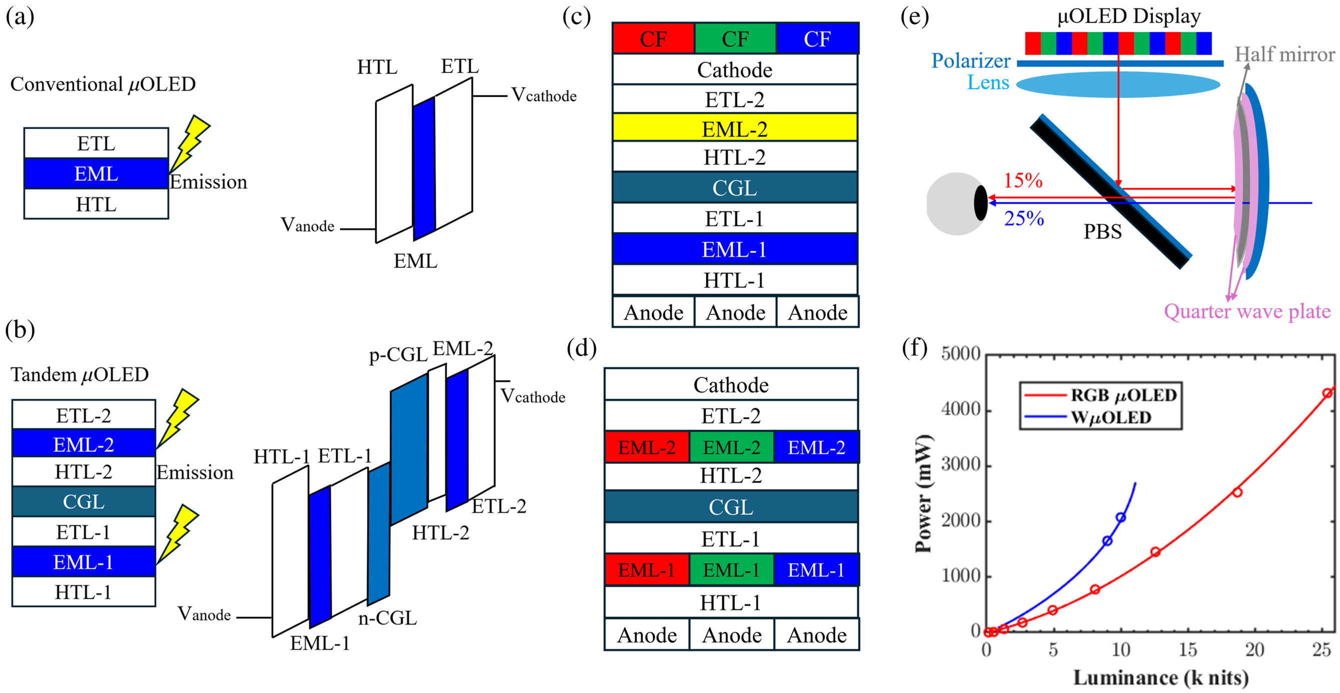

Fig. 5 (a) Working principle of OLED. (b) Working principle of tandem OLED. (c) Schematic of white μOLED. (d) Schematic of RGB μOLED. (e) Schematic of birdbath structure. (f) Power consumption of RGB μOLED and white μOLED. Dots are measured data from Refs. 70 and 71.

PPI.[77] Other techniques, such as maskless lithography[78] and selective area growth of ITO,[79] have been developed for high-resolution monochromatic μOLED displays. In 2016, eMagin introduced a direct-patterned full-color 2645 PPI RGB μOLED with a peak brightness of 11,300 nits.[80] In 2024, Fukuzaki et al. reported a 3207 PPI tandem RGB μOLED fabricated through photolithography.[81] This display demonstrated a luminance decay time (LT90) of 130 h at an initial brightness of 88,000 nits. However, the high cost and scalability of this technology for full-color RGB μOLED mass production still require further validation.

3.2 μOLED-based AR Glasses

The primary challenge for μOLED technology is its low peak luminance, largely due to the instability of organic materials. In a waveguide-based AR system, microdisplays must deliver luminance levels of up to 1,000,000 nits. However, organic bonds would degrade under an excessive current flow,[82] high exciton density,[83] and localized heating,[84] leading to performance degradation. To overcome this problem, μOLED displays are often integrated with freeform optics, such as birdbath optics, which offer a higher optical efficiency (~15%), as shown in Fig. 5(e).[85] The optical loss mainly originates from the absorptive polarizer on top of the OLED panel and the half mirror. Despite this improvement, only about 25% of environmental light reaches the human eye due to the beam splitter and half-mirror configuration. In addition, concerns around weight distribution and bulkiness persist. For instance, the Lenovo ThinkReality A3, released in 2021, weighs 130 g. Although the more recent TCL RayNeo Air 2S reduced the weight to 78 g, the front-heavy design of birdbath optics combined with μOLED displays remains less comfortable than the weight-balanced designs of diffractive waveguide-based AR glasses. Moreover, in birdbath optics, the size of the μOLED panel typically ranges from 0.5″ to 1.0″ (e.g., 0.71″ in LG Nreal) to increase the étendue, which is significantly larger compared with μLEDs used in diffractive waveguide systems.

3.3 Power Consumption

Because μOLED and other light engines employ different projection methods, the comparison of power consumption is typically based on the brightness perceived by the human eye. On the other hand, only 25% of environmental light can be received by the eye, instead of 70% for the optical combiner in waveguide-based systems. Considering ~15% birdbath optical efficiency, then ~9500 nits would be required from the μOLED panel to achieve a similar image readability.[6]

The power consumption calculation for RGB μOLED is similar to that of μLED, with the primary difference being the higher driving voltage due to the tandem structure. According to eMagin's report,[71] a 0.87-in. 1920 × 1200 display can reach a peak luminance of over 25,000 nits. The power consumption of the RGB tandem μOLED is represented by the red curve in Fig. 5(f) for a full-screen white display. To achieve 9500 nits at a 100% duty cycle, the μOLED array consumes ~944 mW. In contrast, the power consumption of white μOLED dramatically doubles to 1813 mW due to the substantial losses from color filters and the reduced μOLED EQE at high current densities [blue line in Fig. 5(f)].[70] To suppress the image blurs of active-matrix display devices, such as LCD, μOLED, and μLED, a low-duty cycle ($\leq 30\%$) is required.[86] Under such a condition, the peak luminance of the microdisplay will be 3.3× higher and neither white μOLED nor RGB tandem μOLED can achieve such a demanding requirement.

4 Liquid-Crystal-on-Silicon (LCoS)

4.1 LCoS Panel

A typical LCoS device consists of a silicon backplane, pixelated aluminum electrodes, an LC layer, an ITO common electrode, and a cover glass, as Fig. 6(a) shows. When the incoming light traverses the LC layer twice, the polarization state can be modulated by voltage-induced LC reorientations. For amplitude-modulating LCoS, an analyzer or a polarizing beam splitter (PBS) is required to convert the phase retardation to amplitude modulation. To achieve a small pixel size, field sequential color (FSC) is widely adopted to eliminate color filters. More specifically, the panel is illuminated by external RGB LEDs and several subframe images are sequentially displayed, which will be integrated into a frame image by human eyes. Figure 6(b) shows two major LC modes: mixed-mode twisted nematic (MTN) and vertical alignment (VA), which are employed in amplitude-modulating LCoS. The former is normally white, and the latter is normally dark. For MTN in the voltage-off state, the LCs are twisted from the bottom substrate to the top substrate, thus changing the polarization state of the incoming light and generating a bright state. The LCs can be reorientated toward a vertical direction by applied voltages, thus generating gray levels. The contrast ratio of the MTN mode is limited to ~1000:1 because the LCs near the substrate are hardly

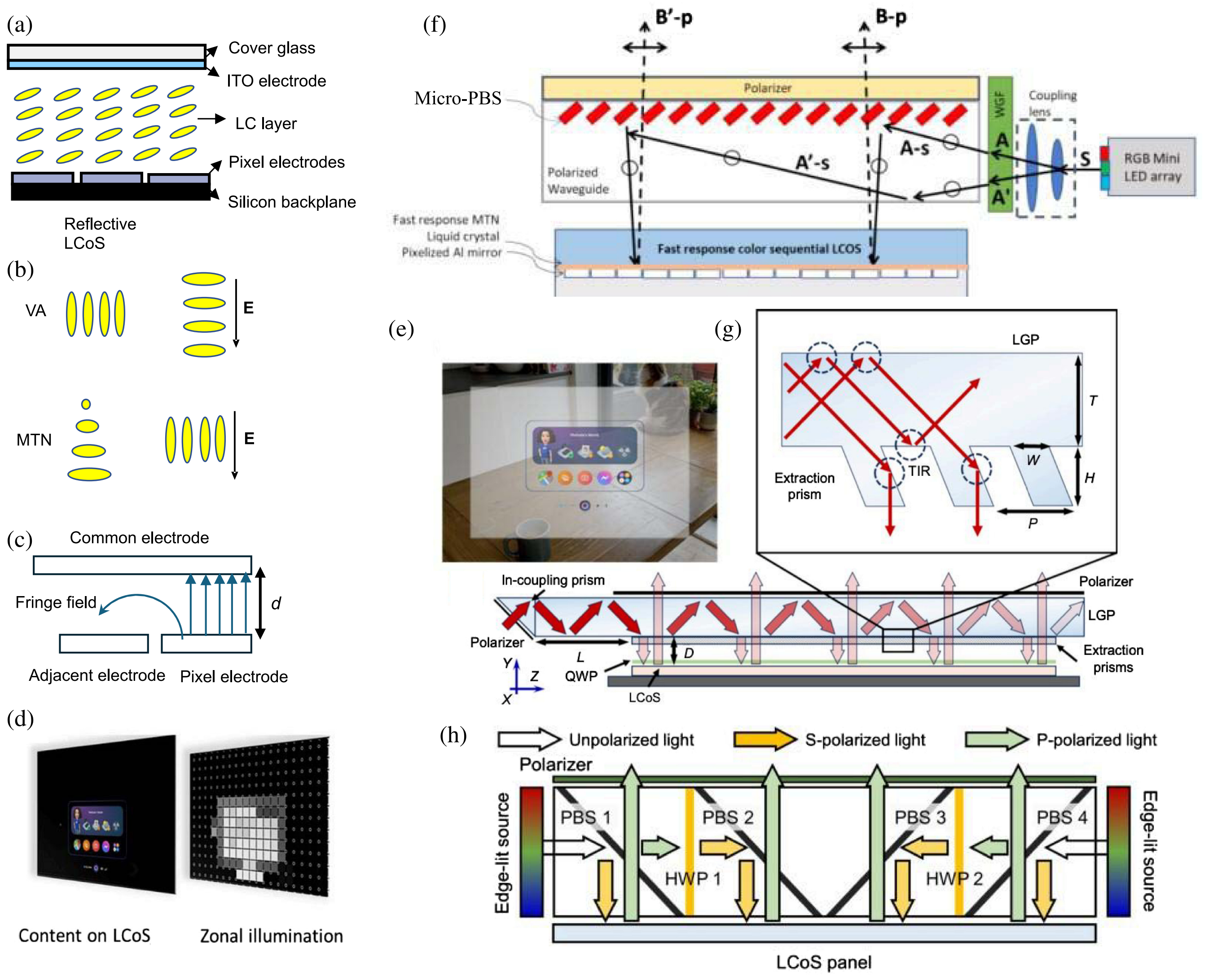

Fig. 6 (a) The architecture of a typical LCoS device. (b) Two major LC modes. (c) Fringe field effect in LCoS devices. (d) Zonal illumination architecture. Reprinted with permission from Ref. 87, © John Wiley and Sons 2024. (e) The schematic of the gray box when the ambient light is not bright. Reprinted with permission from Ref. 87, © John Wiley and Sons 2024. (f) Front-lit illumination developed by Himax. Reprinted with permission from Ref. 92, © John Wiley and Sons 2023. (g) Compact LCoS with novel illumination architecture: in-coupling prism, light guide plate, and extraction prisms. Reprinted from Ref. 93 under a Creative Commons license. (h) Compact LCoS with four thin PBS cuboids and two half-wave plates. Reprinted from Ref. 94 under a Creative Commons license.

reoriented by the voltage owing to strong surface anchoring in the substrate. As a comparison, the dark state for VA mode is achieved without any applied voltage, and thus a high on-axis contrast ratio can be obtained. Despite these advantages, the viewing cone of VA mode is narrower than that of MTN mode, posing a constraint on the collection cone of the projection lens.

When the pixel pitch becomes closer to the cell gap, the fringing field effect (FFE) becomes more severe. Figure 6(c) shows that the fringe field is generated between the voltage-on pixel and the adjacent voltage-off pixel, which decreases the efficiency and contrast ratio for amplitude-modulating LCoS. Although VA mode can exhibit a higher reflectance than MTN mode, its severe FFE reduces the reflectance averaged over the entire pixel. In addition to LC mode-dependent reflectance $R_{\mathrm{LC\,mode}}$ (~80% for MTN after considering FFE), the total LCoS reflectance (optical throughput) is also determined by the mirror reflectance R_{mirror} (~90%), fill factor (FF ~ 95%), and zeroth-order diffraction efficiency $\eta_{\mathrm{diffraction}}$ (~95%), as formulated in Eq. 11.

$$R_{\mathrm{LCoS}} = R_{\mathrm{mirror}} \times \mathrm{FF} \times \eta_{\mathrm{diffraction}} \times R_{\mathrm{LC\,mode}}. \tag{11}$$

Therefore, the total MTN LCoS reflectance is ~65%. To achieve a higher optical throughput, we can employ a distributed Bragg reflector to increase R_{mirror} and reduce inter-pixel gaps to increase the FF and mitigate diffraction losses.

4.2 LCoS Illumination System

In numerous AR scenarios, only one portion of the panel has image contents. In other words, the projected images and videos in AR glasses are usually sparse. However, RGB LEDs in conventional LCoS systems illuminate the entire panel and do not depend on the image contents. To save power consumption, both Avegant and Meta[87,88] proposed to turn on an LED array that only illuminates a certain portion of the LCoS panel with image contents, as shown in Fig. 6(d). The independently controlled (local dimming) zones are required. Compared with direct-view liquid crystal displays (LCDs) with local dimming zones,[89] LCoS requires much smaller LED sizes to achieve the same function. Power saving depends on the image contents, zone design, and zone number. Besides power saving, it can also mitigate the issue of gray boxes. Compared with emissive displays such as μLEDs and tandem μOLEDs, the contrast ratio of LCoS is usually limited, leading to an imperfect dark state. When ambient light is not bright, and the APL of image contents is low, the gray box becomes much more evident as shown in Fig. 6(e). The zonal illuminated architecture can greatly eliminate the gray box by completely turning off the LEDs that originally illuminated the gray box. Finally, the local dimming also enables local primary desaturation (LPD)[90] to mitigate the color breakup (CBU) caused by eye saccade or quick head rotation. This algorithm was originally proposed to suppress the CBU in FSC LCDs[91] and is applicable to FSC LCoS as well. The key point is that the color gamut can be locally shrunk by adopting three desaturated primary colors. It is noted that LPD can increase the luminance by turning on RGB LEDs in each of the three subframes. Although zonal illumination has numerous benefits, how to design illumination systems and increase uniformity while keeping a compact form factor remains challenging.

Owing to its bulky PBS cube, the form factor of LCoS is much larger compared with self-emissive displays. To reduce the volume, Himax developed a front-lit LCoS[92] with a volume of ~0.5 cc by introducing the micro-PBS array, as illustrated in Fig. 6(f). The light beam (S) emitted from the RGB mini-LED array is collimated and split into A and A′ by the coupling lens. Both A and A′ will be s-polarized by the employed wire-grid polarizer. The A-s will directly be reflected by the micro-PBS array toward the LCoS. The A'-s will first experience a total internal reflection, then hit the micromirror array, and is finally reflected toward the LCoS. Owing to the polarization modulation of the LCoS, A-s and A'-s are converted to B-p and B'-p and then passed through the micro-PBS array and the clean-up polarizer, which is used for further improving the contrast ratio. In addition to Himax, Avegant also demonstrated an ultracompact LCoS. However, each approach has its own pros and cons. For example, the optical efficiency of the Himax approach is only ~10% for a linearly polarized light, whereas the contrast ratio of the Avegant method is only about 100:1.

To reduce the volume of LCoS while keeping a high optical efficiency and high contrast ratio, Luo et al.[93] proposed a novel illumination system. The key elements to enable the compact illumination system include an in-coupling prism and a light guide plate (LGP) with multiple parallelepiped extraction prisms, as shown in Fig. 6(g). The in-coupling prism couples the light emitted from the LEDs into the LGP, which will continue to travel inside the LGP owing to total internal reflection. The enlarged figure shows that some of the light beams will hit the extraction prisms and be reflected toward the bottom LCoS and other light beams continue to travel inside the LGP. For an FSC 1024 × 1024 LCoS panel with ~4.4-μm pixel pitch, the simulated optical efficiency using a linearly polarized incident light can reach around 40%, and the volume (without the projection optics) is only ~0.25 cc. To ease the fabrication process, Luo et al. also proposed four thin PBS cuboids to reduce the volume to 25% of the conventional PBS-based system,[94] as shown in Fig. 6(h). The optical efficiency is about 36.7% for an unpolarized input light.

4.3 LCoS Power Consumption

The total power consumption of an LCoS system consists of two parts: electrical power from the CMOS backplane to drive the LC molecules and optical power from the backlight. The electrical power consumption is mainly determined by the APL and LC mode. Different LC modes not only affect the contrast ratio but also lead to content-dependent electrical power consumption. For "normally white" MTN LCoS, a lower APL content (i.e., more pixels are in a dark state) consumes more electrical power because the applied voltage is required to reorientate LCs. To reduce electrical power consumption, Cho et al. presented an 8T static-random-access memory structure to reduce the power of a 0.13-μm CMOS by 78%.[95] Except for the improvements in circuit design, the power consumption for LCoS at the resolution of 1024 × 1024 can be reduced from 200 to 50 mW by improving the CMOS process from 0.18 μm to 55 nm.[92]

The LCoS panel is illuminated by RGB LEDs or a passive matrix (PM) mini-LED array. As stated in Secs. 4.1 and 4.2, the major optical losses come from the limited polarization conversion efficiency of the unpolarized LED array, imperfect reflectance from the LCoS panel, and illumination system. As reported in SID Display Week 2024, the optical efficiency of the Himax's front-lit LCoS is 8.5%, including the LCoS panel and polarization conversion.[92] This optical efficiency is defined by the ratio of total lumen received after the front-lit illumination system versus the collected light (in all angles) emitted from the LED. The LED optical power consumption can be calculated as

$$P_{\mathrm{LED}} = \sum_{n}^{n=R,G,B} \frac{P_{n,\mathrm{Optical}}}{\mathrm{WPE}_n \times \eta_{\mathrm{Duty}} \times \eta_{\mathrm{acceptance}}} = \sum_{n}^{n=R,G,B} \frac{\phi_n}{N_n \times \eta_{n,e} \times \mathrm{WPE}_n \times \eta_{\mathrm{Duty}} \times \eta_{\mathrm{acceptance}}}, \tag{12}$$

where $\eta_{\mathrm{Duty}} = 96\%$ and $\eta_{\mathrm{acceptance}} = 70\%$ correspond to the color sequential duty ratio and ±15 deg acceptance angle of the projection lens, respectively. N_n is the human eye's sensitivity to the light source and $\eta_{n,e}$ corresponds to the system efficiency of the illumination system.

The WPEs of commercial RGB-packed LEDs produced by LumiLED (model L1MC-RGB0028000MP0) are found to be 30.8%, 30.7%, and 57%, respectively. The overall optical efficiency to provide 3-lm white light is calculated to be 781 mW, which is close to the Himax estimated power consumption of 4 lm/W. The total power consumption for the Himax front-lit MTN LCoS to provide 3-lm light is about 831 mW to 781 mW as the APL increases from 0% to 100%. Assuming the polarization recycling efficiency is 70%, Luo's design[93] can further reduce the LED power consumption to only 312 mW to 262 mW.

5 Digital Light Processing (DLP)

5.1 DLP Working Principle

Similar to LCoS, DLP is based on a digital micromirror device (DMD) paired with micro-electro-mechanical system (MEMS) control, developed by Texas Instrument (TI). The DMD is composed of a micromirror array and each micromirror corresponds to a full-color pixel. Figure 7(a) depicts the working principle of DMD.[96] The unpolarized FSC LEDs illuminate the DMD panel, and the on/off state is controlled by the rotation of mirrors. In the voltage-on state, the DMD directs the incident light to the projection lens, whereas in the voltage-off state, the reflected light is absorbed by the coated black paint. In comparison with LCoS, DMD typically has a higher optical efficiency because it can use unpolarized light, except that its illumination system composed of freeform optics is more complicated and bulkier.[98]

5.2 DLP Power Consumption

Similar to LCoS, the power consumption of a DLP projector is divided into two parts: optical power from LEDs and electrical power from MEMS. For TI's DLP3010 with a resolution 1280 × 720 (pixel pitch ≈ 5.4 μm), the electrical power consumption is ranged from 162 to 219 mW. By reducing the pixel pitch to 4.5 μm, the power consumption can be further reduced by 30%.[99]

The optical efficiency is mainly dependent on the DMD efficiency, illumination system efficiency, and multi-layer transmittance. For TI's DLP3010 with 5.4-μm pixel pitch, the DMD efficiency is calculated to be 68% with a consideration of 92% double path window transmission, 93% mirror filling factor, 86% diffraction, and 89% reflectance from mirrors. The illumination system is the most important part of a DLP panel. In 2017, TI proposed an R/B 2-in-1 illumination system for microdisplays and achieved over 70% geometric efficiency by Zemax ray-tracing.[97] However, the illumination optics are still too bulky because two LED panels are included in the system as shown in Fig. 7(b). In 2023, TI proposed a new compact optical architecture by shrinking the illumination light source into a single full-color LED panel and removing the dichroic mirror [Fig. 7(c)]. However, the geometric efficiency of RGB channels is reduced to 42.7%, 40.4%, and 35.7%,[90] respectively. Considering the

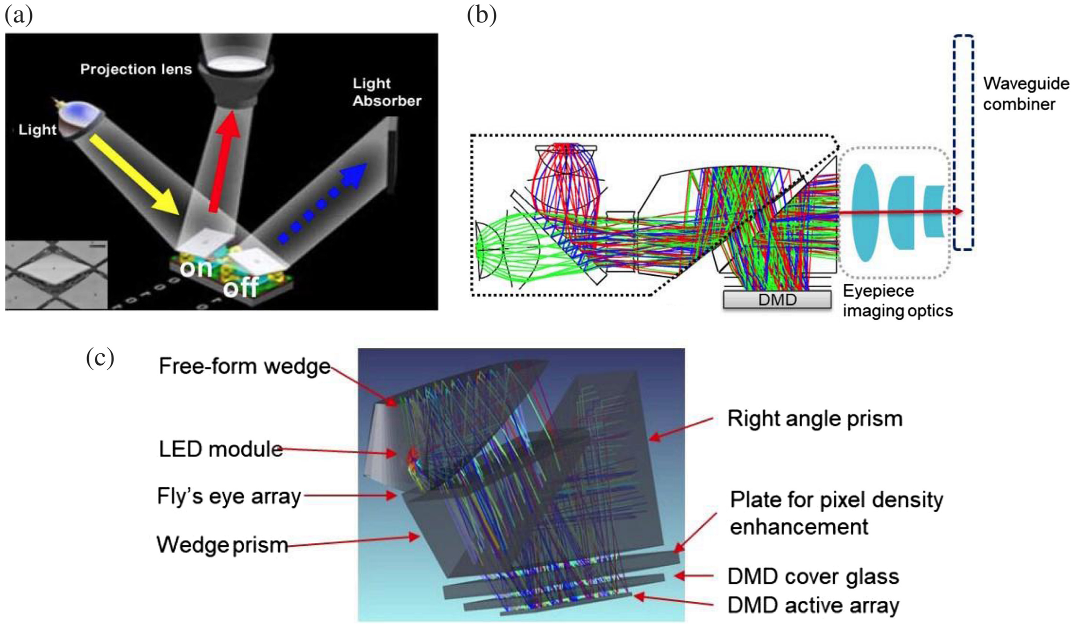

Fig. 7 (a) The architecture of a typical DLP device. Reprinted with permission from Ref. 96, © IEEE 2012. (b) R/B 2-in-1 illumination system.[97] (c) Freeform compact illumination system. (b), (c) Reprinted with permission from Ref. 97, © SPIE 2023.

material absorption and multi-layer transmittance, which is approximated to be 65%, as well as the 68% DMD efficiency, the optical engine efficiency (η_e) for the RGB LEDs is about 18.9%, 17.9%, and 15.8%, respectively. The LED optical power consumption can be calculated as

$$P_{\mathrm{LED}} = \sum_{n}^{n=R,G,B} \frac{P_{n,\mathrm{Optical}}}{\mathrm{WPE}_n \times \eta_{\mathrm{Duty}}} = \sum_{n}^{n=R,G,B} \frac{\phi_n}{N_n \times \eta_{n,e} \times \mathrm{WPE}_n \times \eta_{\mathrm{Duty}}}, \tag{13}$$

where $\eta_{\mathrm{Duty}} = 96\%$ corresponds to the color sequential duty ratio. By considering the WPE of RGB-packed LEDs to be 30.8%, 30.7%, and 57%, respectively, our calculated overall optical efficiency to provide a 3-lm white light is 222.6 mW (i.e., 13.5 lm/W), which is in a very good agreement with the TI's estimated power consumption of 14 lm/W.

6 Laser Beam Scanning (LBS)

6.1 LBS Working Principle

LBS is a mature technology in the realm of augmented reality (AR) displays, offering unique advantages in terms of high brightness, small volume (<0.5 cc), and high power efficiency. An LBS is composed of an RGB laser module and a MEMS scanner. The RGB lasers are combined by dichroic mirrors and packed as described in Fig. 8(a).[101] Different from DLP, the MEMS in LBS is composed of two 1D mirrors or one 2D mirror. From the viewpoint of compactness, one 2D MEMS mirror is preferred as shown in Fig. 8(b), but its driving power consumption is about 10% higher.[102] The MEMS driving power consumption depends on the scanner specifications, such as scan frequencies and product of maximum scan half angle (θ) and mirror diameter (D) (θ-D product). These values are determined by the required display resolution and frame rate.[103,104] The θ-D (unit: deg·mm) of a 1D scanner can be approximated as[105]

$$\theta\text{-}D = \frac{aN\lambda}{4} \times \frac{180}{\pi}, \tag{14}$$

where a is the mirror shape factor ($a = 1$ for rectangular mirror and $a = 1.22$ for circular mirror), N is the number of pixels, and λ is the light wavelength.

6.2 LBS Power Consumption

The power consumption of the LBS system consists of two parts: the laser's optical power consumption and the MEMS scanner's electrical power consumption. Compared with LEDs, laser light sources are more directional with a narrower FWHM,

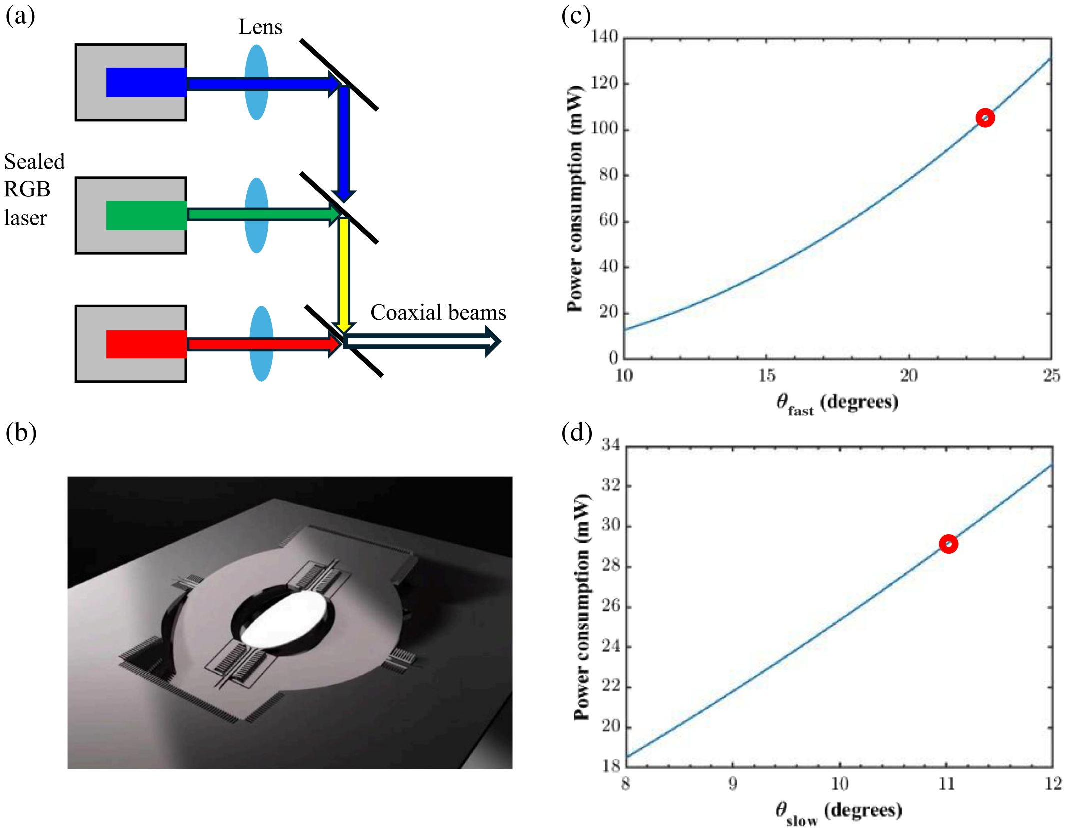

Fig. 8 (a) The architecture of a typical LBS device. (b) OQmented 2D MEMS mirror. Reprinted with permission from Ref. 100, © SPIE 2021. (c) Estimated power consumption of 1 mm fast piezoelectric mirror driving at 35 kHz. (d) Estimated power consumption of 2D piezoelectric mirror slow axis driving at 600 Hz. Red dots indicate the calculated power consumption of OQmented MEMS mirror at resonant conditions.

but the downsides are lower WPE and speckles. The WPE of RGB lasers with emission wavelengths of [640 nm, 532 nm, 450 nm] is [25%, 14%, 10%], respectively.[106] Although both DLP and LBS utilize MEMS, the illumination systems have several differences. Due to a higher directionality, the laser beams are collimated in the illumination system. However, the resolution is proportional to the scan mirror size and scan angle. Therefore, for a high-resolution LBS display, the efficiency may be reduced by a broader modulation transfer function (MTF).[107] For a typical scanning display, the pixel size is chosen at the FWHM of the Gaussian spot[103] and the MTF efficiency (η_{MTF}) is calculated approximately to be 76%. To reduce laser speckles, a despeckle film is typically applied at the input coupler to reduce the coherence and its efficiency $\eta_{\mathrm{despeckle}}$ can approach 80%.[108] To provide a $\phi_n = 3$-lm white light to the input coupler, the power consumption of the laser diodes in MEMS can be calculated as

$$P_{\mathrm{Laser}} = \sum_{n}^{n=R,G,B} \frac{\phi_n}{N_n \times \eta_{n,e} \times \mathrm{WPE}_n \times \eta_{\mathrm{despeckle}} \times \eta_{\mathrm{mirror}} \times \eta_T \times \eta_{\mathrm{MTF}}}, \tag{15}$$

where $\eta_{\mathrm{despeckle}}$, η_{mirror}, η_T, and η_{MTF} represent the efficiency of despeckle film, MEMS mirror, multilayer transmittance, and MTF efficiency, respectively. Considering $\eta_{\mathrm{mirror}} = 85\%$ and $\eta_T = 66\%$, the required laser power is 373 mW for a 2D MEMS mirror.

The power consumption of the MEMS mirror is heavily dependent on the actuation methods, θ-D product, and frame rate. To activate a MEMS mirror, the power consumption is below 10 mW.[109,110] However, due to the high driving voltage requirements, the driving electronics consume significantly more power. In 2007, Kim et al. demonstrated electromagnetic actuation MEMS, achieving a pixel size of 5 μm, a resolution of 1024 × 1024, and a power consumption of 150 mW, though the frame rate was limited to 18.5 Hz.[111] In 2012, Lemoptix used electromagnetic 2D MEMS mirrors to achieve a 1.5 cc micro projector with 100 mW power consumption and 20 kHz scanning rate to achieve a resolution of SVGA (800 × 600) at 60 Hz frame rate.[102] To reduce power consumption, electrostatic actuation based on comb drivers or piezoelectric actuation with AlN actuators is preferred. In 2019, Microsoft introduced the HoloLens 2 with a field of view (FoV) of 43 deg × 29 deg and a resolution of 47 pixels per degree (PPD). This design employed two vertical-stacked lasers per color, with fast mirrors using piezoelectric actuation and slow mirrors using electromagnetic actuation. The power consumption for the entire display and image processing unit was 1 W per panel.[7] In 2022, STMicroelectronics reported that 1D MEMS could reduce the driving voltage from 200 to 17 V by transitioning from electrostatic to piezoelectric actuation. At a resonance frequency of 27.5 kHz, power consumption dropped to 20 mW, though the θ-D product was limited to 15 deg·mm.[112] OQmented reported in 2021 and 2023 SPIE that Lissajous scan 2D MEMS mirrors with a resolution of 2048 × 1024 at a 60 Hz frame rate only consume 200 mW at sparse content.[100,113] Based on Eq. (14), the θ-D product of the 2D circular piezoelectric mirror is 22.73 and 11.36 deg·mm for the fast and slow axis, respectively. The oscillation frequency of the fast and slow axis is 35 kHz and 600 Hz, respectively, to ensure a good image quality. Because the electrical power consumption of MEMS is proportional to the oscillation frequency, and increases with the θ-D product, here, we estimate the electrical power consumption of MEMS based on the measured data.[112] Figures 8(c) and 8(d) indicate that our estimated power consumption of MEMS is 105 mW and 30 mW for the fast and slow axis, respectively. That means, the total MEMS electrical power consumption is 135 mW. Considering the abovementioned 373 mW optical laser power, at the sparse image content (APL ~ 15%), our estimated total power consumption is 135 mW + 373 mW × 0.15 = 191 mW, which is close to the measured data (less than 200 mW) reported by OQmented.

7 Smart Dimmer

The ambient contrast ratio (ACR) of an AR eyewear is defined as

$$\mathrm{ACR} = \frac{L_{\mathrm{on}} + L_{\mathrm{ambient}} \times T}{L_{\mathrm{off}} + L_{\mathrm{ambient}} \times T}, \tag{16}$$

where L_{on}, L_{off}, L_{ambient}, and T represent the on-state display luminance, off-state display luminance, ambient light luminance, and transmittance of the optical combiner. Achieving a high ambient contrast ratio (ACR) is crucial for users, as it enhances the visual sensitivity to image contents.[114] According to Eq. (16), to enhance the ACR of AR eyewear, two approaches can be considered: (1) boosting L_{on} by an adaptive brightness control and (2) adding a smart dimmer to reduce L_{ambient}. The former will undoubtedly lead to increased power consumption, whereas the latter helps to reduce the ambient light.

Two types of smart dimmers have been developed: a single pixel for global dimming and segmented pixels for local dimming. Figures 9(a)–9(c) illustrate the AR eyewear without any dimmer, with a single pixel global dimmer, and with a segmented dimmer,[115] respectively. Using a global dimmer [Fig. 9(b)], the transmittance of the ambient light changes uniformly. For a segmented dimmer, the dimmer consists of several zones so that the transparency of each zone can be individually manipulated by the applied voltage [Fig. 9(c)]. In addition, a smart dimmer is preferred to be “normally transparent” to ensure fail-safe operation. This means in the case of circuit malfunction; the dimmer remains in the see-through state.

In terms of device operation mechanisms, the electrochromic (EC) effect, film-compensated liquid crystal modulator, and dichroic dye-doped liquid crystal have been demonstrated. Figure 9(d) shows the device structure of a global smart dimmer using the EC effect.[116] When a voltage is applied, ions from the storage layer are driven through the ion conductor layer toward the EC layer. Afterward, these ions interact with the EC material and cause a redox reaction with a change in the oxidation state of the EC material, resulting in a transmittance change. In addition, the organic EC material can maintain this final state without applying voltage, which helps to save power. The original state can be reversed by applying an opposite voltage. The transmittance of the bright state and the dark state can achieve 90% and 0.01%, respectively. However, the slow response time (~17 s) of EC materials is a major challenge.[117] To shorten the response time to <1 s, Kortz et al. developed complementary organic EC materials with transparent nano-particle layer electrodes, but the peak transmittance is reduced to ~60%.[118]

The second type of smart dimmer is a film-compensated homogeneous LC cell[119] used in Fig. 9(b). The contrast ratio

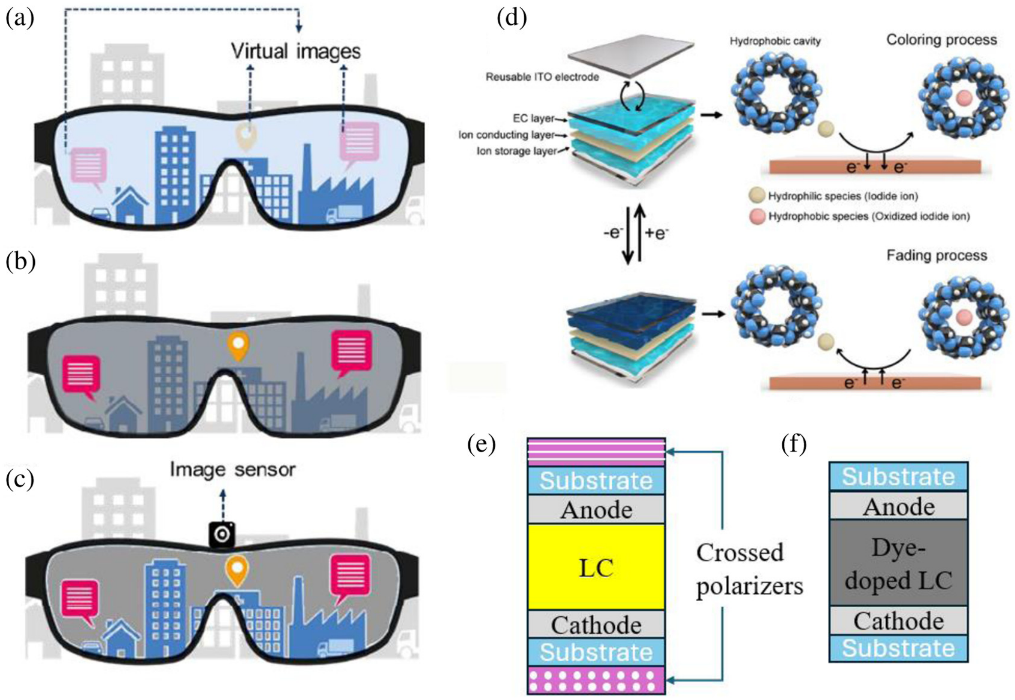

Fig. 9 (a)–(c) Schematic of virtual image quality in AR eyewear (a) without dimmer, (b) with global dimmer, and (c) with pixelated dimmer. Reprinted with permission from Ref. 115, © John Wiley and Sons 2024. (d) The architecture of EC modulation smart window. Reprinted from Ref. 116 under a Creative Commons license. (e) The architecture of film-compensated homogeneous LC smart window. (f) The architecture of dye-doped LC smart window.

is greater than 300:1 and its fast response time (8 ms) enables 120 Hz frame rate. In 2022, such a segmented smart dimmer (~5000 zones; aperture size = 1.57") with a tunable transmittance from 22% to 0.3% has been implemented in Magic Leap 2 to improve the ACR and to enable occlusion.[120] In 2024 SID Display Week, Liqxtal Technology reported a high contrast LC dimmer with 33% bright state transmittance and 0.1% dark state transmittance.[115] To mitigate the diffraction patterns caused by the periodic pixels, they applied an S-curved scan and data lines with an impressive 96% aperture ratio.

The third type is dichroic dye-doped LC cell [Fig. 9(c)] whose major advantage is polarization independence. However, the contrast ratio is typically <5:1 for a single-layer device because of the limited dichroic ratio of the dyes. In 2016, Zhu et al. first proposed a fast-response guest-host LC dimmer for AR displays with a transmittance tunable from 73% to 26%.[121] In 2024, Liqxtal Technology also reported a dye-doped LC dimmer with 56% bright-state transmittance and 16% dark-state transmittance.[115] By optimizing the dye material and concentration, LC cell gap, and device structure, the transmittance range can be extended from ~70% to ~10% or even wider.

The performance of all three types of smart dimmers is summarized in Table 1. The electrochromic effect can offer an excellent contrast ratio, but its response time is relatively slow. By contrast, LC-based smart dimmers have a much faster response time to enable real-time dynamic dimming; especially, the film-compensated LC dimmer provides both high contrast and fast response time and is useful for enhancing the immersion of AR eyewear. On the other hand, the major advantage of a dye-doped LC smart dimmer is its polarization independence.

8 Conclusions and Outlook

We have reviewed the recent advancements and challenges of six microdisplay light engines, particularly focusing on their power consumption. Table 2 summarizes their advantages, challenges, and possible solutions.

Figure 10(a) shows a comparison of our calculated power consumption of existing light engines based on 3-lm luminous power received at the in-coupler produced by a 1000 × 1000 resolution microdisplay light engine. Considering both power consumption and image quality, a monochromatic μLED

Table 1 Performance of three types of smart dimmers. The LC dimmer data are taken from Ref. 115.

	Electrochromic	Film-compensated LC	Dye-doped LC
Bright state transmittance	60%	33%	70%
Dark state transmittance	0.01%	0.1%	10%
Contrast ratio	6000:1	330:1	7:1
Response time (ms)	~1100	8	12

Table 2 Advantages, challenges, and possible solutions of six presented light engines.

	Advantages	Challenges	Solutions
3-panel μLED	High efficiency of green monochromatic display.	Alignment of RGB colors.	Monolithic integration.
	Image quality.	Low efficiency for red color.	CMQW structure.
	Long lifetime.	High power consumption of driving IC.	Advanced CMOS process.
QDCC μLED	Easier fabrication for single-color panel.	Stability and lifetime.	Surface and material engineering.
	Wide color gamut.	Low conversion efficiency.	
μOLED	High-resolution density (6000 PPI).	Require birdbath optics due to insufficient brightness.	RGB OLED with improved mask fabrication.
		Low efficiency at high current.	
		Bulkiness.	
LCoS	High stability.	Compactness and efficiency trade-off.	Novel illumination architecture.
	Mature technology.	Require a polarized light source.	
	Low cost.		
DLP	High optical efficiency.	Difficult to further reduce pixel size.	Novel illumination architecture.
		Bulky illumination system.	
LBS	High optical efficiency.	Poor image quality.	Additional compensation film.
	Low power consumption of MEMS mirrors.	Limited frame rate.	Faster resonance of piezoelectric actuation.

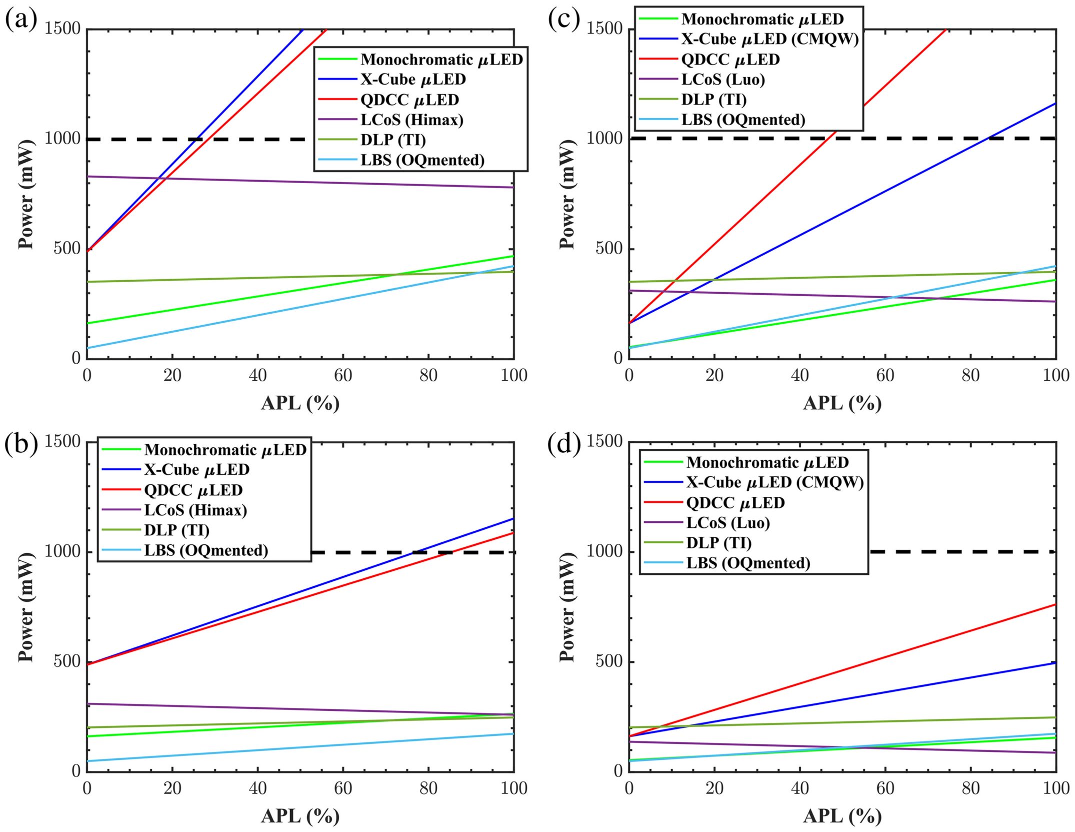

Fig. 10 (a), (b) Calculated power consumption of commonly employed microdisplay light engines for AR glasses at the current stage when producing (a) 3-lm and (b) 1-lm luminous power. (c), (d) Calculated power consumption of microdisplay light engines with improved architectures when producing (c) 3-lm and (d) 1-lm luminous power. CMQW stands for JBD's continuous MQW.

display is an attractive option for entry-level lightweight AR glasses. For the X-cube–based full-color μLED, constraining the power consumption below 1 W to prevent overheating would undoubtedly limit the image content to APL $\leq$ 30%. Under the same scenarios, LCoS, LBS, and DLP can meet such criterion at APL $=$ 100%, which represents the case of web browsers.

Implementing a smart dimmer helps to reduce power consumption and improve the ambient contrast ratio. If the ambient light transmittance can be reduced to 10%, then the display brightness of 1300 nits is adequate to achieve a 4:1 ambient contrast ratio, which is equivalent to coupling 1-lm luminous power into the in-coupler of the waveguide. In this scenario, the electrical power consumption remains the same, but the optical power consumption can be reduced to 1/3 of the original value. As described in Fig. 10(b), all the light engines are capable of avoiding the overheating threshold of 1 W/panel.

Both μLED and LCoS hold great potential to be the ultimate solutions for next-generation AR glasses if the power consumption can be further reduced as shown in Figs. 10(c) and 10(d) without and with smart dimmer, respectively. For μLED driving IC, the power consumption can be further reduced by using an advanced CMOS process to decrease the operating voltage and adopting a power management IC to shut down unused blocks and adjust the frequency and voltage based on the display content.[122] By replacing 0.18-μm CMOS with 55-nm CMOS, the power consumption can be reduced by $\sim 3\times$. For X-cube–based μLEDs, the major challenge comes from the low efficiency of small-size AlGaInP red μLED. By implementing JBD's novel continuous MQW design, which shows 8% WPE, the power consumption can be significantly reduced. With the help of a smart dimmer, it is possible to avoid overheating in outdoor conditions, even for "normally dark" circuit design. For the QDCC μLED, the photostability issue must be overcome before it can be considered further for practical applications. In the case of LCoS, the novel front-lit design from Luo et al.[85] can greatly reduce the power consumption to a level lower than DLP. By further implementing local dimming, the power consumption can be even lower than that of LBS. For DLP, the remaining challenges are in the fabrication of small micro-mirrors, the reduced optical efficiency for small pixels, and the increased overall system volume because of the employed freeform optics. LBS remains the most power-efficient light engine for microdisplays due to its highly collimated laser source and low-power piezoelectric MEMS actuation, whereas its limited frame rate and raster-scanned image quality require further improvement.

Disclosures

The authors declare no conflicts of interest.

Code and Data Availability

Code, data, and materials are available upon request from the corresponding author.

Author Contributions

Y.Q. initiated the project. Y.Q., Z.Y., S.-C.C., Y.M, Y.-C.C., and H.-S.C. (NTHU) conducted the simulation and wrote the manuscript. C.-L.L. (NCKU) and S.-T.W. supervised the project and edited the manuscript.

Acknowledgements

The authors are indebted to AUO Corporation and Nichia for partial financial supports.

References

1. E.-L. Hsiang et al., "AR/VR light engines: perspectives and challenges," *Adv. Opt. Photonics* **14**(4), 783–861 (2022).
2. K. Matsuhashi, T. Kanamoto, and A. Kurokawa, "Thermal model and countermeasures for future smart glasses," *Sensors* **20**(5), 1446 (2020).
3. J. Xiong et al., "Augmented reality and virtual reality displays: emerging technologies and future perspectives," *Light Sci. Appl.* **10**, 216 (2021).
4. Y. Ding et al., "Waveguide-based augmented reality displays: perspectives and challenges," *eLight* **3**, 24 (2023).
5. Y. Ding et al., "Breaking the in-coupling efficiency limit in waveguide-based AR displays with polarization volume gratings," *Light Sci. Appl.* **13**, 185 (2024).
6. Y. Qian et al., "Enhancing a display's sunlight readability with tone mapping," *Photonics* **11**(6), 578 (2024).
7. P. Skurowski et al., "Energy demand in AR applications-a reverse ablation study of the HoloLens 2 device," *Energies* **17**(3), 553 (2024).
8. L. Qi et al., "848 PPI high-brightness active-matrix micro-LED micro-display using GaN-on-Si epi-wafers towards mass production," *Opt. Express* **29**(7), 10580–10591 (2021).
9. F. Olivier et al., "Shockley-Read-Hall and Auger non-radiative recombination in GaN based LEDs: a size effect study," *Appl. Phys. Lett.* **111**, 022104 (2017).
10. Y. Huang et al., "Mini-LED, micro-LED and OLED displays: present status and future perspectives," *Light Sci. Appl.* **9**, 105 (2020).
11. C.-C. Lin et al., "The micro-LED roadmap: status quo and prospects," *J. Phys. Photonics* **5**(4), 042502 (2023).
12. D. Armitage, I. Underwood, and S.-T. Wu, *Introduction to Microdisplays*, John Wiley & Sons (2006).
13. J. Seong et al., "CMOS backplane pixel circuit with leakage and voltage drop compensation for an micro-LED display achieving 5000 PPI or higher," *IEEE Access* **8**, 49467–49476 (2020).
14. S.-S. Cheng and P. C.-P. Chao, "A high 6318-PPI pixel circuit that realizes 10-bit gray levels for analog-PWM driven micro-LED displays," *IEEE Trans. Electron Dev.* **71**(2), 1122–1130 (2024).
15. S.-S. Cheng and P. C.-P. Chao, "A new SRAM-embedded pixel circuit that modulates accurately gray level for PWM-driven micro-LED displays," *IEEE Solid-State Circuits Lett.* **6**, 157–160 (2023).
16. S.-S. Cheng and P. C.-P. Chao, "A high 5292-PPI pixel circuit for micro displays with 10-bit gray levels realized via the technique of analog sub-frame integral," *IEEE Trans. Electron Dev.* **11**, 456–466 (2023).
17. Y.-Z. Lin et al. "Active-matrix micro-LED display driven by metal oxide TFTs using digital PWM method," *IEEE Trans. Electron Dev.* **68**(11), 5656–5661 (2021).
18. A. M. N. Elahi et al., "Thermal and photochemical stability studies of color-converted microLED microdisplay panels," *IEEE Photonics J.* **15**(3), 7000206 (2023).
19. W. Zeng et al., "P-27: a novel pixel circuit with threshold voltage variation compensation in three-dimensional AMOLED on silicon microdisplay," in *SID Symp. Digest Tech. Papers*, Vol. **50**, pp. 1313–1316 (2019).
20. W. S. Tan and Q. Li, "4-1: invited paper: industrializing microled microdisplays for AR applications," in *SID Symp. Digest Tech. Papers*, Vol. **54**, pp. 21–24 (2023).
21. Y. Motoyama et al., "High-efficiency OLED microdisplay with microlens array," *J. Soc. Inf. Disp.* **27**(6), 669–675 (2019).

22. K.-L. Liang et al., "Advances in color-converted micro-LED arrays," *Jpn. J. Appl. Phys.* **60**, SA0802 (2020).
23. Y. Boussadi et al., "Investigation of sidewall damage induced by reactive ion etching on AlGaInP mesa for micro-LED application," *J. Lumin.* **234**, 117937 (2021).
24. J. M. Smith et al., "Comparison of size-dependent characteristics of blue and green InGaN microLEDs down to 1 μm in diameter," *Appl. Phys. Lett.* **116**, 071102 (2020).
25. Y. Yang and X. Cao, "Removing plasma-induced sidewall damage in GaN-based light-emitting diodes by annealing and wet chemical treatments," *J. Vac. Sci. Technol. B* **27**(6), 2337–2341 (2009).
26. W. Chen et al., "High-performance, single-pyramid micro light-emitting diode with leakage current confinement layer," *Appl. Phys. Express* **8**(3), 032102 (2015).
27. M. S. Wong et al., "High efficiency of III-nitride micro-light-emitting diodes by sidewall passivation using atomic layer deposition," *Opt. Express* **26**(16), 21324–21331 (2018).
28. M. S. Wong et al., "Size-independent peak efficiency of III-nitride micro-light-emitting-diodes using chemical treatment and sidewall passivation," *Appl. Phys. Express* **12**(9), 097004 (2019).
29. Y. Qian et al., "High-efficiency vertical-chip micro-light-emitting diodes via p-GaN optimization and surface passivation," *Crystals* **14**(6), 503 (2024).
30. Y.-H. Hsu et al., "Current confinement effect on the performance of blue light micro-LEDs with 10 μm dimension," *ACS Omega* **8**(38), 35351–35358 (2023).
31. Y. Kato et al., "Selective growth of wurtzite GaN and $Al_xGa_{1-x}N$ on GaN/sapphire substrates by metalorganic vapor phase epitaxy," *J. Cryst. Growth* **144**(3–4), 133–140 (1994).
32. A. Pandey et al., "A red-emitting micrometer scale LED with external quantum efficiency >8%," *Appl. Phys. Lett.* **122**(15), 151103 (2023).
33. Q. Li et al., "11-1: invited paper: microLED displays for augmented reality smart glasses," in *SID Symp. Digest Tech. Papers*, Vol. **55**, pp. 104–107 (2024).
34. M.-C. Wu, M.-C. Chung, and C.-Y. Wu, "3200 PPI matrix-addressable blue microLED display," *Micromachines* **13**(8), 1350 (2022).
35. H. Wu et al., "Ultra-high brightness micro-LEDs with wafer-scale uniform GaN-on-silicon epilayers," *Light Sci. Appl.* **13**, 284 (2024).
36. F. Templier, "GaN-based emissive microdisplays: a very promising technology for compact, ultra-high brightness display systems," *J. Soc. Inf. Disp.* **24**(11), 669–675 (2016).
37. X. Ji et al., "3400 PPI active-matrix monolithic blue and green micro-LED Display," *IEEE Trans. Electron Devices* **70**(9), 4689–4693 (2023).
38. K.-P. Chang et al., "High performance AlGaInP-based micro-LED displays with novel pixel structures," *IEEE Photonic Technol. Lett.* **33**(24), 1375–1378 (2021).
39. P. Feng et al., "A simple approach to achieving ultrasmall III-nitride microlight-emitting diodes with red emission," *ACS Appl. Electron. Mater.* **4**(6), 2787–2792 (2022).
40. J. Flemish et al., "38-3: invited paper: microLED device technology for low-power wearable displays," in *SID Symp. Digest Tech. Papers*, Vol. **53**, pp. 478–480 (2022).
41. K. Fan et al., "Analysis of size-dependent optoelectronic properties of red AlGaInP micro-LEDs," *Opt. Express* **31**(22), 36293–36303 (2023).
42. M.-C. Wu, Z.-L. Hsu, and C.-Y. Wu, "High-pixel-density 960 × 540 flip-chip AlGaInP red microLED display," *IEEE Trans. Electron Dev.* **69**(11), 6206–6211 (2022).
43. J.-K. Cho and M. Jeong, "A low-power digital pixel driving scheme for single-pulse-PWM-based display using AND-embedded pixel circuits," *IEEE Trans. Circuit Syst. Video Technol.* **29**(11), 3382–3392 (2018).
44. Y. Wu et al., "Full-color realization of micro-LED displays," *Nanomaterials* **10**(12), 2482 (2020).
45. S. H. Mun et al., "Highly efficient full-color inorganic LEDs on a single wafer by using multiple adhesive bonding," *Adv. Mater. Interfaces* **8**(14), 2100300 (2021).
46. P. Chen and Q. Li, "55-4: invited paper: monolithic microLED display for AR applications," in *SID Symp. Digest Tech. Papers*, Vol. **54**, pp. 1874–1877 (2023).
47. International Committee for Display Metrology, *Information Display Measurements Standard*, Society for Information Display (SID), Campbell, CA, USA (2012).
48. G.-H. Chen et al., "General strategies for preparing hybrid polymer/quantum dot nanocomposites for color conversion," *Nanomaterials* **13**(23), 3072 (2023).
49. C.-L. Wu et al., "11-2: invited paper: full color microLED micro-display technology for AR applications with μ-pixeled solutions," in *SID Symp. Digest Tech. Papers*, Vol. 55, pp. 108–110 (2024).
50. G.-H. Chen et al., "Enhanced photostability of core/shell quantum dots under intense blue light irradiation through positive photoaging mechanism," *ACS Appl. Mater. Interfaces* **15**(45), 52795–52805 (2023).
51. C.-W. Yeh et al., "Inhibiting the surface oxidation of low-cadmim-content ZnS:(Cd, Se) quantum dots for enhancing application reliability," *ACS Appl. Nano Mater.* **2**(8), 5290–5301 (2019).
52. S.-J. Ho et al., "Inkjet-printed salt-encapsulated quantum dot film for UV-based RGB color-converted micro-light emitting diode displays," *ACS Appl. Mater. Interfaces* **12**(29), 33346–33351 (2020).
53. H. Park et al., "Efficient quantum dot color conversion layer with mixed spherical/rod-shaped scattering particles," *ACS Appl. Opt. Mater.* **1**(1), 289–297 (2023).
54. I. J. L. Plante et al., "55-2: invited paper: quantum dot color conversion for displays," in *SID Symp. Digest Tech. Papers*, Vol. **54**, pp. 792–794 (2023).
55. P. Yang et al., "High-resolution inkjet printing of quantum dot light-emitting microdiode arrays," *Adv. Opt. Mater.* **8**(1), 1901429 (2020).
56. Y.-H. Ra et al., "Full-color single nanowire pixels for projection displays," *Nano Lett.* **16**(7), 4608–4615 (2016).
57. Z. Li et al., "Review on III-V semiconductor nanowire array infrared photodetectors," *Adv. Mater. Technol.* **8**(13), 2202126 (2023).
58. A. Pandey and Z. Mi, "Multi-wavelength nanowire micro-LEDs for future high speed optical communication," *Opto-Electron. Adv.* **7**, 240011 (2024).
59. K. Tomioka et al., "Selective-area growth of III-V nanowires and their applications," *J. Mater. Res.* **26**(17), 2127–2141 (2011).
60. R. G. Hobbs, N. Petkov, and J. D. Holmes, "Semiconductor nanowire fabrication by bottom-up and top-down paradigms," *Chem. Mater.* **24**(11), 1975–1991 (2012).
61. Y. Qian et al., "Directional high-efficiency nanowire LEDs with reduced angular color shift for AR and VR displays," *Opto-Electron Sci.* **1**(12), 220021 (2022).
62. I.-C. Robin et al., "52-2: invited paper: 1 μm nanowire based microLED chips for efficient and high performance smart watch displays," in *SID Symp. Digest Tech. Papers*, Vol. **55**, pp. 709–712 (2024).
63. A. Pandey et al., "An ultrahigh efficiency excitonic micro-LED," *Nano Lett.* **23**(5), 1680–1687 (2023).
64. M. Hartensveld, "Proposal and realization of V-groove color tunable μLEDs," *Opt. Express* **30**(15), 27314–27321 (2022).
65. M. Hartensveld, "InGaN color tunable full color passive matrix," *IEEE Electron Device Lett.* **44**(3), 460–463 (2023).
66. K. Hui, P. Lai, and H. Choi, "Vertically-stacked color-tunable LEDs," *Phys. Status Solidi C* **6**(S2), S902–S904 (2009).

67. K. Yadavalli, C.-L. Chuang, and H. S. El-Ghoroury, "Monolithic and heterogeneous integration of RGB micro-LED arrays with pixel-level optics array and CMOS image processor to enable small form-factor display applications," *Proc. SPIE* **11310**, 113100Z (2020).
68. J. Shin et al., "Vertical full-colour micro-LEDs via 2D materials-based layer transfer," *Nature* **614**, 81–87 (2023).
69. H. Jin et al., "Vertically stacked RGB LEDs with optimized distributed Bragg reflectors," *Opt. Lett.* **45**(24), 6671–6674 (2020).
70. J. Jo et al., "High-luminance, large-size 4K OLED microdisplays for VR/MR applications," *J. Soc. Inf. Disp.* **32**(5), 371–378 (2024).
71. A. Ghosh et al., "Developing the world's brightest WUXGA OLED microdisplay," *Inf. Disp.* **38**(2), 19–23 (2022).
72. L. Liao, K. P. Klubek, and C. W. Tang, "High-efficiency tandem organic light-emitting diodes," *Appl. Phys. Lett.* **84**(2), 167–169 (2004).
73. M. K. Fung, Y. Q. Li, and L. S. Liao, "Tandem organic light-emitting diodes," *Adv. Mater.* **28**(47), 10381–10408 (2016).
74. Z. Yang et al., "Advances and challenges in microdisplays and imaging optics for virtual reality and mixed reality," *Device* **2**(6), 100398 (2024).
75. T. Fujii et al., "4032 PPI high-resolution OLED microdisplay," *J. Soc. Inf. Disp.* **26**(3), 178–186 (2018).
76. G. Tan et al., "Analysis and optimization on the angular color shift of RGB OLED displays," *Opt. Express* **25**(26), 33629–33642 (2017).
77. W. Jung et al., "Direct laser patterning of glass mask for micro display using GHz bursts," *J. Soc. Inf. Disp.* **32**(5), 426–434 (2024).
78. K. Kim et al., "High-resolution electrohydrodynamic jet printing of small-molecule organic light-emitting diodes," *Nanoscale* **7**, 13410–13415 (2015).
79. J. Zhu et al., "Micro organic light-emitting diodes fabricated through area-selective growth," *Mater. Chem. Front.* **1**, 2606–2612 (2017).
80. A. Ghosh et al., "62-1: invited paper: directly patterened 2645 PPI full color OLED microdisplay for head mounted wearables," in *SID Symp. Digest Tech. Papers*, Vol. **47**, pp. 837–840 (2016).
81. S. Fukuzaki et al., "High-luminance and highly reliable tandem OLED display including new intermediate connector designed for photolithography applications," *J. Soc. Inf. Disp.* **32**(5), 309–319 (2024).
82. M. Ishii and Y. Taga, "Influence of temperature and drive current on degradation mechanisms in organic light-emitting diodes," *Appl. Phys. Lett.* **80**(18), 3430–3432 (2002).
83. H. Yu et al., "Exciton-induced degradation of carbazole-based host materials and its role in the electroluminescence spectral changes in phosphorescent organic light emitting devices with electrical aging," *ACS Appl. Mater. Interfaces* **9**(16), 14145–14152 (2017).
84. P. Tyagi et al., "Degradation of organic light emitting diode: heat related issues and solutions," *Synthetic Metals* **216**, 40–50 (2016).
85. K. Guttag, "Nreal teardown: part 2, detailed look inside," https://kguttag.com/2021/06/04/nreal-teardown-part-2-detailed-look-inside/ (accessed January 2025).
86. F. Peng et al., "Analytical equation for the motion picture response time of display devices," *J. Appl. Phys.* **121**(2), 023108 (2017).
87. F. Peng et al., "19-1: invited paper: zonal illuminated non-emissive displays for AR glass," in *SID Symp. Digest Tech. Papers*, Vol. **55**, pp. 220–222 (2024).
88. E. Tang, "Spotlight display technology: world's first adaptive LED illumination LCoS architecture," *Proc. SPIE* **12914**, 129140M (2023).
89. Z. Yang et al., "Performance comparison between mini-LED backlit LCD and OLED display for 15.6-inch notebook computers," *Appl. Sci.* **12**(3), 1239 (2022).
90. Y. Zhang, F. C. Lin, and E. H. Langendijk, "A field-sequential-color display with a local-primary-desaturation backlight scheme," *J. Soc. Inf. Disp.* **19**(3), 258–264 (2011).
91. Z. Yang et al., "Reducing the power consumption of VR displays with a field sequential color LCD," *Appl. Sci.* **13**(4), 2635 (2023).
92. Y.-W. Li et al., "13-1: invited paper: front-lit LCoS for AR displays," in *SID Symp. Digest Tech. Papers*, Vol. **54**, pp. 154–157 (2023).
93. Z. Luo et al., "Ultracompact and high-efficiency liquid-crystal-on-silicon light engines for augmented reality glasses," *Opto-Electron Adv.* **7**(10), 240039 (2024).
94. Z. Luo et al., "Compact and high-efficiency liquid-crystal-on-silicon for augmented reality displays," *Photonics* **11**, 669 (2024).
95. J.-K. Cho and J. Minsu, "A low-voltage-driven high-voltage SRAM pixel circuit for power reduction in a digital micro-display panel," *IEEE Trans. Circuits I* **67**(5), 1640–1652 (2020).
96. S. C. Shin et al., "The compact systems design based on DMD and the straight line 2-channel LED for a mobile embedded pico projector," *J. Disp. Technol.* **8**(4), 219–224 (2012).
97. Z. Sheng, X. Zhou, and S. Shaw, "Compact digital micromirror device (DMD)-based optical architecture for augmented reality (AR) glasses," *Proc. SPIE* **12435**, 124350A (2023).
98. D. S. Dewald et al., "8-1: invited paper: the Avegant Glyph: optical design considerations and approach to near-eye display," in *SID Symp. Digest Tech. Papers*, Vol. **47**, pp. 69–71 (2016).
99. A. Lakshminarayanan and J. Richuso, "The next generation of DLP Pico technology for AR displays," *Proc. SPIE* **12913**, 1291300 (2024).
100. O. Petrak et al., "Laser beam scanning based AR-display applying resonant 2D MEMS mirrors," *Proc. SPIE* **11765**, 1176503 (2021).
101. J. Reitterer et al., "Ultra-compact micro-electro-mechanical laser beam scanner for augmented reality applications," *Proc. SPIE* **11765**, 1176504 (2021).
102. L. Kilcher and N. Abelé, "MEMS-based microprojection system with a 1.5 cc optical engine," *Proc. SPIE* **8252**, 825204 (2012).
103. H. Urey, D. W. Wine, and T. D. Osborn, "Optical performance requirements for MEMS-scanner-based microdisplays," *Proc. SPIE* **4178**, 176–185 (2000).
104. J. Tauscher et al., "Evolution of MEMS scanning mirrors for laser projection in compact consumer electronics," *Proc. SPIE* **7594**, 75940A (2010).
105. H. Urey, D. W. Wine, and J. R. Lewis, "Scanner design and resolution trade-offs for miniature scanning displays," *Proc. SPIE* **3636**, 60–68 (1999).
106. S. Essaian and J. Khaydarov, "State of the art of compact green lasers for mobile projectors," *Opt. Rev.* **19**, 400–404 (2012).
107. H. Urey et al., "Optics designs and system MTF for laser scanning displays," *Proc. SPIE* **3689**, 238–248 (1999).
108. A. Dwivedi, G. S. Khan, and A. Sharma, "Design and evaluation of laser spot illuminator for a laser projection engine design," *Opt. Eng.* **55**(11), 115102 (2016).
109. M. Lara-Castro et al., "Design and modeling of polysilicon electrothermal actuators for a MEMS mirror with low power consumption," *Micromachines* **8**(7), 203 (2017).
110. K. H. Koh and C. Lee, "A two-dimensional MEMS scanning mirror using hybrid actuation mechanisms with low operation voltage," *J. Microelectromech. Syst.* **21**(5), 1124–1135 (2012).
111. K. H. Kim et al., "Two-axis magnetically-driven MEMS scanning catheter for endoscopic high-speed optical coherence tomography," *Opt. Express* **15**(26), 18130–18140 (2007).
112. N. Boni et al., "Piezoelectric MEMS mirrors for the next generation of small form factor AR glasses," *Proc. SPIE* **12013**, 1201305 (2022).
113. U. Hofmann, "MEMS and laser based microdisplay light engine for AR," *Proc. SPIE* **12914**, 129140X (2024).

114. Y. Qian et al., "Human eye contrast sensitivity to vehicle displays under strong ambient light," *Crystals* **13**(9), 1384 (2023).
115. H.-S. Chen et al., "35-1: invited paper: smart pixelated dimmer for high ambient contrast AR displays," in *SID Symp. Digest Tech. Papers*, Vol. **55**, pp. 447–449 (2024).
116. Y. Wang et al., "Sustainable, low-cost, high-contrast electrochromic displays via host–guest interactions," *Proc. Natl. Acad. Sci.* **121**(18), e2401060121 (2024).
117. Z. Jia et al., "Electrochromic windows with fast response and wide dynamic range for visible-light modulation without traditional electrodes," *Nat. Commun.* **15**, 6110 (2024).
118. C. Kortz et al., "Complementary hybrid electrodes for high contrast electrochromic devices with fast response," *Nat. Commun.* **10**, 4874 (2019).
119. S.-T. Wu and C.-S. Wu, "Optimization of film-compensated homogeneous cells for liquid crystal displays," *Liq. Cryst.* **24**(6), 811–818 (1998).
120. D. Manly et al., "Ghost image mitigation in see-through displays with pixel arrays," U.S. patent 11,169,380 (9 November 2021).
121. R. Zhu et al., "High-ambient-contrast augmented reality with a tunable transmittance liquid crystal film and a functional reflective polarizer," *J. Soc. Inf. Disp.* **24**(4), 229–233 (2016).
122. C. Shi et al., "A highly integrated power management IC for advanced mobile applications," *IEEE J. Solid-State Circuits* **42**(8), 1723–1731 (2007).

Yizhou Qian is a PhD candidate at the University of Central Florida. He received his BS and MEng degrees in electrical engineering from Virginia Tech in 2018 and 2021, respectively. His current research interests include microdisplay light engine, automotive display, and transparent display.

Zhiyong Yang is presently an optical engineer at Meta Reality Labs. He received his BS degree in optoelectronic engineering from Chongqing University in 2017, MS degree in optics and photonic from the University of Michigan in 2019, and PhD in optics from University of Central Florida in 2024. His research interests include AR and VR displays.

Sung-Chun Chen was a visiting PhD student at the University of Central Florida in 2024. He received his BS degree in electrical engineering from National Cheng Kung University, Tainan, Taiwan, in 2019, where he is currently pursuing his PhD in electrical engineering. His research focuses on the system circuit design for micro-LED and AMOLED displays.

Yongziyan Ma received her BS and MS degrees in physics from Capital Normal University in 2017 and 2020, respectively. She is currently working toward a PhD at the College of Optics and Photonics, University of Central Florida. Her current research interests include microdisplay light engines, diffractive optical combiners, and display systems.

Yi-Chien Chen is presently a visiting PhD student at the University of Central Florida. He received his BS degree in electrical engineering in 2020 from National Central University, Taoyuan, Taiwan. He is currently working toward a PhD in electrical engineering at the National Cheng Kung University. His research focuses on the system circuit design for micro-LED and AMOLED displays and external compensation algorithm for displays.

Hsueh-Shih Chen is a professor at the Department of Materials Science and Engineering, National Tsing Hua University, Hsinchu, Taiwan. In 2024, he spent several months as a visiting professor at the University of Central Florida. He received his PhD in materials chemistry from the University of Cambridge, UK, in 2009. His current research interests include quantum dot materials and display devices.

Chih-Lung Lin received his BS and PhD degrees in electrical engineering from National Taiwan University, Taiwan, in 1993 and 1999, respectively. He was a visiting professor at the University of Central Florida. From 2020 to 2023, he was the chair of Department of Electrical Engineering, National Cheng Kung University. He is a fellow of Optica, SID, and IET. His research focuses on micro-LED pixel circuits for AR/VR displays and AI for ePaper driving waveforms and biomedical electronic systems.

Shin-Tson Wu is a trustee chair professor at the College of Optics and Photonics, University of Central Florida (UCF). He received his PhD in physics from the University of Southern California and his BS degree in physics from National Taiwan University. He is an academician of Academia Sinica, a charter fellow of the US National Academy of Inventors, a member of the Academy of Science, Engineering and Medicine of Florida, one of the first six inductees to the Florida Inventors Hall of Fame, and a fellow of the IEEE, OSA, SID, and SPIE. He is a recipient of the SID Lawrence Tannas Award (2025), UCF inaugural Medal of Societal Impact (2024), Optica (formerly OSA) Edwin H. Land Medal (2022), SPIE Maria Goeppert-Mayer Award (2022), OSA Esther Hoffman Beller Medal (2014), SID Slottow-Owaki Prize (2011), OSA Joseph Fraunhofer Award (2010), SPIE G. G. Stokes Award (2008), and SID Jan Rajchman Prize (2008).